

THE COMPLETE ULTRAVIOLET SPECTRUM OF THE ARCHETYPAL “WIND-DOMINATED” QUASAR MRK 231:  
ABSORPTION AND EMISSION FROM A HIGH-SPEED DUSTY NUCLEAR OUTFLOWS. VEILLEUX<sup>1,2</sup>, M. MELÉNDEZ<sup>1,3,4</sup>, T. M. TRIPP<sup>5</sup>, F. HAMANN<sup>6,7</sup>, & D. S. N. RUPKE<sup>8</sup>*Draft version May 4, 2016*

## ABSTRACT

New near- and far-ultraviolet (NUV and FUV) *HST* spectra of Mrk 231, the nearest quasar known, are combined with ground-based optical spectra to study the remarkable dichotomy between the FUV and NUV-optical spectral regions in this object. The FUV emission-line features are faint, broad, and highly blueshifted (up to  $\sim 7000 \text{ km s}^{-1}$ ), with no significant accompanying absorption. In contrast, the profiles of the NUV absorption features resemble those of the optical Na I D, He I, and Ca II H and K lines, exhibiting broad blueshifted troughs that overlap in velocity space with the FUV emission-line features and indicate a dusty, high-density and patchy broad absorption line (BAL) screen covering  $\sim 90\%$  of the observed continuum source at a distance  $\lesssim 2 - 20 \text{ pc}$ . The FUV continuum emission does not show the presence of any obvious stellar features and is remarkably flat compared with the steeply declining NUV continuum. The NUV (FUV) features and continuum emission have not varied significantly over the past  $\sim 22$  (3) years and are unresolved on scales  $\sim 40$  (170) pc. These results favor an AGN origin for the NUV – FUV line and continuum emission. The observed FUV line emission is produced in the outflowing BAL cloud system, while the Balmer lines arise primarily from the standard broad line region seen through the dusty BAL screen. Our data are inconsistent with the recently proposed binary black hole model. We argue instead that Mrk 231 is the nearest example of weak-lined “wind-dominated” quasars with high Eddington ratios and geometrically thick (“slim”) accretion disks; these quasars are likely more common in the early universe.

*Subject headings:* accretion, accretion disks — galaxies: active — quasars: absorption lines — quasars: emission lines — quasars: individual (Mrk 231)

## 1. INTRODUCTION

Observations and numerical simulations have shown that galactic winds play a crucial role in the story of galaxy evolution (see Veilleux, Cecil, & Bland-Hawthorn 2005; Fabian 2012 for reviews). They are the primary mechanism by which matter, energy, and metals are recycled in galaxies and are deposited into the surrounding circumgalactic, intracluster, or intergalactic medium (CGM, ICM, or IGM, respectively; e.g., Tumlinson et al. 2011; Tripp et al. 2011; Werk et al. 2013, 2014; Rubin et al. 2014, 2015; Prochaska et al. 2014; Lau et al. 2015, and references therein). Galactic winds may also quench star formation by heating the cool gas and/or ejecting it from the host. For instance, only a few percent of the radiative energy liberated by the growth of a supermassive black hole (SMBH) needs to be tapped in this way to truncate star formation and the growth of the stellar mass. These “quasar-mode” outflows are distinct from “radio-mode” jets in that they are much less collimated, and therefore have the potential to impact a much greater swath of a galaxy’s gas. Quasar-mode outflows are often invoked to play a fundamental role in the evolution of both SMBHs and their host

galaxies, quenching star formation and regulating black hole growth. They may be at the origin of the tight SMBH – galaxy relations (e.g., Murray, Quataert, & Thompson 2005; Di Matteo, Springel, & Hernquist 2005) and possibly also the cutoff of the galaxy mass function at the high stellar mass end (e.g., Croton et al. 2006; Hopkins et al. 2008).

Direct observational evidence for large-scale quasar mode feedback in galaxies, near and far, has grown dramatically in recent years (molecular gas phase: e.g., Veilleux et al. 2013b; Spoon et al. 2013; Cicone et al. 2014; Gonzalez-Alfonso et al. 2016; neutral and ionized gas phases: e.g., Maiolino et al. 2012; Rupke & Veilleux 2013; Harrison et al. 2014; Zakamska & Greene 2014; Cicone et al. 2015; Cresci et al. 2015; Brusa et al. 2016; Zakamska et al. 2015, 2016). Mrk 231, the focus of the present paper, is the nearest quasar known ( $z = 0.0422$ , corresponding to a distance<sup>9</sup> of 178 Mpc, or  $1'' = 0.863 \text{ kpc}$ ) and arguably the best laboratory to study this quasar feedback in action. It is experiencing a powerful multi-phase and multi-scale outflow that has the potential to rapidly transform the host gas-rich galaxy merger remnant into a “red and dead” spheroidal galaxy (e.g., Rupke et al. 2005; Fischer et al. 2010; Sturm et al. 2011; Rupke & Veilleux 2011, 2013; Veilleux et al. 2014; Aalto et al. 2012; Cicone et al. 2012; Feruglio et al. 2010; 2015; Alatalo 2015; Lindberg et al. 2016, and references therein).

Mrk 231 was the first target observed under our Cycle 19 far-ultraviolet (FUV) spectroscopic survey of the nearby *QUEST* (Quasar – ULIRG Evolution Study; e.g., Veilleux 2012 and references therein) QSOs with the Cosmic Origins Spectrometer (COS) on board the *Hubble Space Telescope* (*HST*). The unprecedented sensitivity of COS allowed us to

<sup>1</sup> Department of Astronomy, University of Maryland, College Park, MD 20742, USA; veilleux@astro.umd.edu

<sup>2</sup> Joint Space-Science Institute, University of Maryland, College Park, MD 20742, USA

<sup>3</sup> NASA Goddard Space Flight Center, Greenbelt, MD 20771, USA

<sup>4</sup> Wyle Science, Technology and Engineering Group, 1290 Hercules Avenue, Houston, TX 77058 USA

<sup>5</sup> Department of Astronomy, University of Massachusetts, Amherst, MA 01003, USA

<sup>6</sup> Department of Physics and Astronomy, University of California, Riverside, CA 92507, USA

<sup>7</sup> Department of Physics & Astronomy, University of California, Riverside, CA 92521, USA

<sup>8</sup> Department of Physics, Rhodes College, Memphis, TN 38112, USA

<sup>9</sup> For a cosmology with  $H_0 = 73 \text{ km s}^{-1} \text{ Mpc}^{-1}$ ,  $\Omega_{\text{matter}} = 0.27$ , and  $\Omega_{\text{vacuum}} = 0.73$ .

obtain the first high-S/N spectrum of Mrk 231 below  $\sim 1500$  Å (Veilleux et al. 2013a; hereafter Paper I). This spectrum is highly peculiar, highlighted by the presence of faint ( $\lesssim 2\%$  of predictions based on H $\alpha$ ), broad ( $\gtrsim 10,000$  km s $^{-1}$  at the base), and highly blueshifted (centroid at  $\sim -3000$  km s $^{-1}$ ) Ly $\alpha$  emission (all velocities reported in this paper are in the reference frame of the quasar, where  $v = 0$  km s $^{-1}$  at redshift  $z = 0.0422$ , derived from CO and H I observations; Downes & Solomon 1998; Carilli et al. 1998). The FUV continuum emission does not show the presence of any obvious photospheric or wind stellar features (e.g., James et al. 2014) and is remarkably flat compared with the steeply declining NUV continuum (Smith et al. 1995; Paper I; Leighly et al. 2014).

Surprisingly, the FUV spectrum also does not show any unambiguous broad absorption features. This is unexpected because the core of Mrk 231 harbors well-known spatially unresolved broad absorption-line (BAL) systems in the optical and near-ultraviolet bands (Boksenberg et al. 1977; Smith et al. 1995; Rupke, Veilleux, & Sanders 2002; Gallagher et al. 2002, 2005). The Mrk 231 BAL features are detected in several transitions including many low-ionization species (e.g., Na I D  $\lambda\lambda 5890, 5896$ , He I\*  $\lambda 3889$ , Ca II H and K, Mg II  $\lambda\lambda 2796, 2803$ , and Mg I  $\lambda 2853$ , as well as Fe II UV1 and Fe II UV2, hence fitting the rare FeLoBAL category). They show strong absorption across the range  $\sim -3500$  to  $-5500$  km s $^{-1}$  and no significant absorption at velocities above  $-3500$  km s $^{-1}$  (e.g., Rupke et al. 2002; Paper I). The absence of narrow ISM lines or stellar P-Cygni profiles in the COS spectrum suggests that the FUV continuum is dominated by AGN emission. However, the BAL features, which are usually attributed to AGN-driven outflows, are also not evident in the FUV spectrum (Paper I). This suggests that the BAL outflow is highly dusty but is also patchy so that the FUV flux can leak through the FeLoBAL screen without having BAL features imprinted on the spectrum. The conclusion that dust plays virtually no role in the FUV is supported by the flatness of the FUV continuum and the near-zero polarization at these wavelengths measured from spectropolarimetric data with the Faint Object Spectrograph (FOS; Smith et al. 1995). The observed Ly $\alpha$  emission is best explained if it is produced in the outflowing BAL cloud system, while the Balmer lines arise primarily from the standard broad emission line region (BELR) seen through the dusty ( $A_V \sim 7$  mag.<sup>10</sup>) broad absorption line region (BALR).

Many of these results were explained in Paper I using a simple spherical geometry or a physically motivated but slightly more complex disk geometry (Figures 5 and 6 in Paper I). However, it was noted that the lack of a contemporaneous high-S/N spectrum covering the diagnostic-rich region from  $1500$  Å to  $3000$  Å was a major hindrance to further interpretation (a 1992 pre-COSTAR FOS NUV spectrum at  $2500 - 3300$  Å published by Smith et al. 1995 was used in the analysis of Paper I). We recently addressed this problem with the acquisition in 2014 of high-S/N FUV and NUV spectra with *HST* COS and STIS, respectively, as well as near-contemporaneous ground-based optical spectra with the 4.3-meter Discovery Channel Telescope (DCT). This paper reports the results of our analysis of these new spectra and com-

parisons with the data used in Paper I. The acquisition and reduction of the *HST* and DCT spectra are discussed in Section 2. The results derived from the new data and comparisons with the old data are described in Section 3. The geometrical models proposed in Paper I are revisited in Section 4, using the additional constraints provided by the new data as well as recent results in the literature. The results are also compared against the predictions from the binary AGN model recently proposed to explain the ultraviolet spectrum of this object by Yan et al. (2015).

## 2. OBSERVATIONS

### 2.1. HST Ultraviolet Spectroscopy

Mrk 231 was revisited using the G140L grating on COS (6 orbits on 2014 December 13) and the G230L grating on STIS (1 orbit on 2014 July 1). The first 5 orbits of the COS/G140L observations were centered at  $1280$  Å, while the other COS orbit was centered at  $1105$  Å to cover the redshifted Ly $\alpha$  region (which is in the chip gap at  $1280$  Å). Overall, the COS spectra cover  $\sim 1100 - 1900$  Å ( $\sim 1050 - 1825$  Å in the rest frame) at a spectral resolving power of  $R = (\lambda/\delta\lambda) \sim 2000 - 5000$ . The STIS spectrum covers the NUV range from  $1800 - 3180$  Å ( $1750 - 3050$  Å in the rest frame) at a spectral resolving power of  $R \sim 500$ , which is sufficient to characterize the BEL and BAL systems in the NUV lines. Note that the Cycle 19 COS spectrum from Paper I was obtained with G130M and therefore had a higher spectral resolution but more limited spectral coverage ( $\sim 1150 - 1470$  Å) than the new COS spectrum.

The COS observations used standard target acquisition procedures. For STIS, we used F28X500II to center on the bluest part of the spectrum to minimize possible (but unlikely for this QSO) centroid shifts between the NUV and optical positions. All of the COS observations were done in TIME-TAG mode. The target exposures were split into four segments using focal-plane splits. This observing strategy was adopted to reduce the fixed pattern noise. The total exposure times were 12,300 seconds at  $1280$  Å and 2660 seconds at  $1105$  Å. The STIS exposures were also split into four segments of equal length (473 seconds to take maximum use of the visibility), for a total exposure time of 1892 seconds.

All observations were processed using both the standard *calcos*<sup>11</sup> calibration pipeline and a custom-made pipeline put together by one of us (T.M.T.) to optimize the quality of the resulting data. The results from both pipelines were found to be nearly identical (the data presented in this paper are from the custom-made pipeline).

### 2.2. Ground-based Optical Spectroscopy

To minimize the effects of spectral variability (e.g., the highest-velocity component of the BAL systems in Mrk 231 at  $\sim -8000$  km s $^{-1}$  is known to be time-variable; Hutchings & Neff 1987; Boroson et al. 1991; Kollatschny et al. 1992; Forster et al. 1995; Rupke et al. 2002, 2005), we acquired a new optical spectrum of this object to complement our 2001, 2004, 2007, and 2012 spectra published in Rupke et al. (2002), Rupke et al. (2005c), Rupke & Veilleux (2011), and Paper I, respectively. The deVeny spectrograph on the 4.3-meter DCT was used on 2015 June 8 and 9 with the  $300$  g

<sup>10</sup> Leighly et al. (2014) have argued that the amount of extinction may be as low as  $A_V \sim 1.5 - 1.6$  mag. when applying the reddening curve of Goodbar (2008), previously used to explain low values of total-to-selective extinctions in Type Ia supernovae.

<sup>11</sup> See Chapter 3 of Part II of the *HST* Data Handbook for COS (<http://www.stsci.edu/hst/cos/documents/handbooks/datahandbook>) for the details of the *calcos* processing.

mm<sup>-1</sup> grating in the first order and a 1.''5 slit to obtain 8 spectra each of 5 min duration with a spectral resolving power of  $\sim 920$ , covering  $\sim 3530 - 8000$  Å. Standard IRAF<sup>12</sup> procedures were used to reduce and calibrate these spectra. The sky conditions were not photometric and the flux calibration below 5500 Å was found to be unreliable so this portion of the DCT spectrum is not discussed here.

### 3. RESULTS

The 2014 Cycle 21 HST/COS and STIS spectra of Mrk 231 are shown in Figures 1-4 along with the 2011 October 15 Cycle 19 HST/COS spectrum, the 2015 DCT/deVeny optical spectrum, and the 2001 Keck/ESI optical spectrum for comparison. The line measurements derived from these data are listed in Table 1.

Figure 1 shows that the 2011 and 2014 COS spectra are remarkably similar: there is no evidence for any variations in the FUV continuum level and slope, within the uncertainties of the measurements. At both epochs, the FUV continuum from  $\sim 1100 - 1700$  Å (rest frame) declines slightly at shorter wavelengths, following  $F_\lambda \propto \lambda^{\alpha_\lambda}$  where  $\alpha_\lambda = 0.7 \pm 0.3$  using anchor regions at [1298 – 1304], [1416 – 1418] and [1508 – 1515] Å ( $\alpha_\lambda$  increases to  $\sim 1.7$  when considering only the continuum below Ly $\alpha$ ; see Paper I). Similarly, we find no evidence for change in the Ly $\alpha$  profile between 2011 and 2014, within the uncertainties of our measurements (dominated by uncertainties in the continuum placement and difference in spectral resolution between the two observations).

The profile of the Ly $\alpha$  emission, shown in detail in Figure 5, has remained highly peculiar, showing a narrow peak centered at  $\sim 1261$  Å ( $\sim -1500$  km s<sup>-1</sup> in the rest frame) and wings extending over at least 1240 – 1265 Å ( $\sim 6000$  km s<sup>-1</sup>) and quite possibly as much as 1225 – 1280 Å ( $\sim 13,000$  km s<sup>-1</sup>). The overall centroid of the Ly $\alpha$  emission is blueshifted by  $\sim 3000$  km s<sup>-1</sup> with respect to rest (given the absence of Si II  $\lambda 1260$  and O I  $\lambda 1302$  emission, Si II  $\lambda \lambda 1190, 1193, \text{N I } \lambda 1200$ , and Si III  $\lambda 1207$  emission do not affect the profile of Ly $\alpha$ ). The broad width and large blueshift clearly point to an AGN origin for this feature. This is made clear in Figure 5, where we compare the profile of Ly $\alpha$  with those of H $\alpha$  emission and Na I D  $\lambda \lambda 5890, 5896$  absorption, derived from the most recent DCT data. Since we find no evidence for significant changes in the profiles of H $\alpha$  and Na I D since 2001 (Rupke et al. 2002), we also show in Figure 5 the profiles of He I\*  $\lambda 3889$  and Ca II H and K derived from these older data (Na I D is distinctly broader than these features because it is a blended doublet transition). The high velocities of these features are consistent with material originating close to the central black hole. Indeed, the Ly $\alpha$  emission is centered on the NUV nucleus and spatially unresolved with the rather coarse spatial resolution of COS at 1250 Å for our settings ( $\sim 1.''3 \sim 1.1$  kpc; Ghavamian et al. 2010). Similarly, the broad H $\alpha$  emission and highly blueshifted Na I D troughs are spatially unresolved ( $\lesssim 0.''6 \sim 500$  pc) in the ground-based IFU data of Rupke & Veilleux (2011, 2013). Better constraints on the size of the source of FUV-NUV emission are derived from the excellent match in the overlap region between the new COS and STIS spectra (see below).

As noted in Paper I, the Ly $\alpha$  emission is also much fainter relative to H $\alpha$  than the prediction from Case B recombination

(Ly $\alpha$ /H $\alpha \sim 0.05$  instead of the expected  $\sim 13$ ). While collisional suppression of the level 2 population in hydrogen is known to reduce Ly $\alpha$ /H $\alpha$  ratio by a factor of up to  $\sim 2 - 3$  relative to the Case B value in the high-density BELRs of quasars (e.g., Netzer et al. 1995), the more extreme Ly $\alpha$ /H $\alpha$  ratio of Mrk 231 is likely due to Ly $\alpha$  absorption by dust grains. This conclusion seems inescapable when considering the gas at  $v \geq 0$  km s<sup>-1</sup> where Ly $\alpha$ /H $\alpha$  is even more extreme. This issue is revisited in Section 4.

The new COS data confirm the dearth of clearly identifiable features, other than Ly $\alpha$ , within the wavelength coverage of the 2011 COS spectrum (see Table 1 in Paper I for a list of tentative identifications for the various “bumps” and “wiggles” seen in the 2011 spectrum and also seen in the recent spectrum). However, the new COS/G140L spectrum now extends to  $\sim 1900$  Å and shows a significant detection of the C IV  $\lambda \lambda 1548, 1550$  emission feature (Figure 1). This feature appears purely in emission, and is broad ( $\sim 6000$  km s<sup>-1</sup>) and highly blueshifted ( $\sim 3250$  km s<sup>-1</sup>), i.e. similar to the Ly $\alpha$  emission profile (see comparison in Fig. 6). The C IV absorption reported by Gallagher et al. (2002) in the 1992 FOS data is not present in the newer 2014 data. The detected C IV emission is faint, representing only  $\sim 20\%$  of the (faint) Ly $\alpha$  emission (Table 1).

The new STIS spectrum presented in Figure 2 also shows the presence of faint, highly blueshifted C III]  $\lambda 1908.7$  line emission with a profile that resembles that of Ly $\alpha$  (Fig. 6). As first pointed out by Smith et al. (1995) and Gallagher et al. (2002), and shown in Figure 6, one has to be careful when interpreting this emission feature since there are several other transitions in this wavelength region that may potentially contaminate the C III] profile. The absence of Fe III UV 34  $\lambda 1926.3$  suggests that the Fe III UV 34 multiplet transitions at 1895.5 and 1914.1 Å do not significantly affect the profile of C III]. Similarly, Si III]  $\lambda 1892.0$  is unlikely to be important as it is generally undetected or much fainter than C III] and Fe III in BAL quasars (e.g., Hartig & Baldwin 1986; Hall et al. 2002; although it can be strong in non-BAL quasars: e.g., Laor et al. 1997 in I Zw 1 and Baldwin et al. 1996 in a sample of narrow-line quasars). Finally, Al III  $\lambda \lambda 1854.7, 1862.8$  are too far to the blue to significantly affect the bulk of the C III] profile (only perhaps the extreme blue wing).

For the sake of completeness, we also show in Figure 6 the continuum-subtracted emission near the expected location of C II  $\lambda 1334$ . As pointed out in Paper I, the S/N ratio here is low and continuum placement is tricky, making this detection only tentative. However, we note that the profile of this faint emission is similar within the uncertainties to that of the other FUV lines, providing tantalizing evidence for blueshifted C II  $\lambda 1334$  emission in this spectrum.

As first noted by Smith et al. (1995), and discussed in detail in Paper I and Leighly et al. (2014), a dramatic upturn in the spectral energy distribution (SED) is seen above  $\sim 2200$  Å (Fig. 4). Remarkably, the spectrum longward of this wavelength is also rich in deep blueshifted absorption troughs, in stark contrast with the few faint and blueshifted emission lines detected in the FUV. The main NUV features detected in the STIS spectrum are the broad absorptions lines from He I  $\lambda 2945.1$ , Mg I  $\lambda 2852.9$ , Mg II  $\lambda \lambda 2796.3, 2803.4$ , and the Fe II UV1 UV2, UV3, UV61, UV62, UV63, and UV78 multiplets. The strongest of these features are labeled in Figures 2 and 3 and shown in velocity space in Figure 7. The purpose of this last figure is not to compare the profiles point-by-point,

<sup>12</sup> <http://iraf.noao.edu/>



since these features range in complexity from single transitions (He I and Mg I), blended doublet (Mg II), and multiple transitions from various ground and excited states making a detailed comparison meaningless, but to emphasize that all of features are produced in the outflowing material. These features are common in the rest-frame UV spectra of FeLoBAL quasars (e.g., Hall et al. 2002; Lucy et al. 2014), and all of them except Fe II UV3, UV60, UV61, and UV78 were identified in the 1992 FOS spectrum first presented by Smith et al. (1995). The presence of broad absorption features from various excited states provides important constraints on the properties of the BALR. We return to this point at the end of Section 4.2.

A direct comparison between the 2014 STIS NUV spectrum and the 1992 FOS spectra obtained by Smith et al. (1995) is made difficult by the limited S/N and significant ( $\geq 30\%$ ) light losses of the aberrated pre-COSTAR FOS data. Figure 2 shows a comparison after heavily smoothing the FOS data and scaling them to try to account for these light losses and reproduce the spectra shown in Figure 1 of Smith et al. Interestingly, the 2014 STIS NUV spectrum obtained through a  $0''.2 \times 50''$  aperture is remarkably similar to the 1992 FOS spectra obtained through an effective aperture of  $4''.3 \times 1''.4$ . The limited S/N of the FOS data does not allow us to carry out a detailed analysis of the various features in these data, but a visual comparison of the two spectra does not reveal any significant differences in the various absorption features. This indicates that the NUV continuum emission and BAL features have remained constant over a period of at least  $\sim 22$  years and are spatially unresolved on a scale of  $\lesssim 0''.2 \sim 170$  pc. The NUV target acquisition images obtained in both Cycles 19 and 21 are consistent with an unresolved point source centered on the optical position of the quasar at the resolution of the COS imager (intrinsic FWHM  $\lesssim 2$  pixels  $\sim 0''.05 \sim 40$  pc). Similarly, all of the NUV continuum and line emission is unresolved along the slit in the STIS spectrum (intrinsic FWHM  $\lesssim 1$  pixel  $\sim 0''.05 \sim 40$  pc). Finally, we note that the flux level of the 2014 STIS NUV spectrum obtained with the  $0''.2 \times 50''$  aperture is consistent with that of the 2014 COS FUV spectrum obtained with a  $2''.5 \times 2''.5$  aperture in the overlap region. Barring fortuitous counteracting effects, this suggests that not only is the NUV emission unresolved on scales below  $\sim 170$  pc scale but also the FUV emission. This is another argument in favor of an AGN origin for both the NUV and FUV continuum emission.

#### 4. DISCUSSION

The new FUV, NUV, and optical spectra presented in this paper add strong new constraints on the structure and geometry of the BELR, BALR, and source of continuum emission in Mrk 231. First, in Section 4.1, we compare the UV line and continuum properties of Mrk 231 with those of other quasars, drawing an analogy with PHL-1811 analogs and weak-lined quasars (WLQs). Next, in Section 4.2, we revisit the geometrical models presented in Paper I to interpret the new data. Finally, in Section 4.3, we confront the predictions from the binary AGN scenario proposed by Yan et al. (2015) with the results of our analysis of the new data.

##### 4.1. Far-Ultraviolet Properties of Mrk 231 in the Broader Context

As recently pointed out by Teng et al. (2014), Mrk 231 is an outlier among quasars, in the sense that it is weaker in the X-rays than typical quasars: the total absorption-corrected AGN

luminosity for Mrk 231 in  $0.5 - 30$  keV is only  $\sim 1.0 \times 10^{43}$  erg s $^{-1}$ . Compared to  $L_{\text{bol,AGN}}$  of  $1.1 \times 10^{46}$  erg s $^{-1}$  (Veilleux et al. 2009), the  $2 - 10$  keV X-ray luminosity is only 0.03–0.05% of the AGN bolometric luminosity. This ratio is typically  $\sim 2$  to 15% among radio-quiet quasars, with the most luminous objects typically having the lowest ratios. However, X-ray weakness is common among Seyfert 1-like ULIRGs (Teng & Veilleux 2010), LoBAL QSOs (Luo et al. 2013), PHL-1811 analogs (Leighly et al. 2007a,b; Wu et al. 2011), and other “wind dominated” weak-lined quasars (WLQs; Luo et al. 2015). Evidence for significant X-ray absorption is present in many of these objects, particularly the PHL-1811 analogs and WLQs (Luo et al. 2015), but not in PHL 1811 itself (Leighly et al. 2007a), nor Mrk 231 (Teng et al. 2014).

Interestingly, the accretion rate in many of these X-ray faint objects also appear to be large, sometimes formally above the Eddington value, based on the best black hole mass estimates. This also seems to be the case for Mrk 231. Assuming the dynamically derived black hole mass of  $1.7^{+4.0}_{-1.2} \times 10^7 M_{\odot}$  based on stellar velocity dispersions measured from near-infrared spectra (Dasyra et al. 2006), the Eddington ratio of the AGN in Mrk 231 is  $5.0^{+11.3}_{-3.5}$ . The  $\sim 5 \times$  higher value of  $M_{\text{BH}}$  from Kawakatu et al. (2007) would bring the Eddington ratio closer to unity; this mass measurement is derived from the H $\beta$  line width and optical continuum and is considered an upper limit because it was taken using a  $3''$  aperture and is no doubt affected by continuum-light contamination from the host. More recently, Leighly et al. (2014) derived a black hole mass  $M_{\text{BH}} = 2.3 \times 10^8 M_{\odot}$  from the width of broad Pa $\alpha$  and the  $1 \mu\text{m}$  luminosity density (using the prescription of Landt et al. 2013); this results in an Eddington ratio of  $\sim 0.3$ . Sources with near or super-Eddington accretion rates are expected to drive nuclear outflows. Mrk 231 fits the mold given its FeLoBAL characteristics, indicative of a nuclear outflow of up to  $8000 \text{ km s}^{-1}$ , and tentatively detected ultra-fast X-ray wind of  $20,000 \text{ km s}^{-1}$  (Feruglio et al. 2015).

Our new FUV data indicate that Mrk 231 shares at least two additional properties with these fast accreting X-ray weak objects: the FUV emission lines of Mrk 231 are weak relative to the continuum and highly blueshifted. As listed in Table 1, the equivalent width of C IV measured in Mrk 231 is only 12 Å. That is  $\sim 3 \times$  smaller than the typical value of luminous SDSS quasars ( $30.0 \pm 0.03$  Å; e.g., Vanden Berk et al. 2001; Richards et al. 2011). Given the well-known Baldwin effect (i.e. quasars of lower luminosities present larger C IV equivalent widths on average), the difference in EW(C IV) between Mrk 231 and quasars of comparable luminosities is actually even larger. Similarly, the blueshift of  $\sim 3000 \text{ km s}^{-1}$  of the Ly $\alpha$ , C IV, and C III] lines in Mrk 231 falls well above the distribution of velocities in radio-quiet and radio-loud quasars (e.g., Fig. 2 of Richards et al. 2011). In contrast, C IV equivalent widths  $\lesssim 12$  Å and blueshifts  $\gtrsim 1000 \text{ km s}^{-1}$  are common in PHL 1811 analogs (Leighly et al. 2007b; Wu et al. 2011) and in WLQs (Luo et al. 2015). Moreover, Plotkin et al. (2015) have recently shown that the low-ionization lines of H $\alpha$  and H $\beta$  in PHL-1811 analogs and WLQs are not exceptionally weak, in contrast to their high-ionization lines like C IV. Mrk 231 also shows very weak to no high-ionization line emission in the optical (e.g., He II 4686 Å, [O III] 5007 Å; e.g., Rupke et al. 2002), near-infrared (e.g., [Si VI]  $1.96 \mu\text{m}$ ; Leighly et al. 2014), or mid-infrared (e.g., [O IV]  $25.89 \mu\text{m}$ , [Ne V]  $14.32, 24.32 \mu\text{m}$ , [Ne VI]  $7.65 \mu\text{m}$ ; Armus et al.

2007), but relatively normal low-ionization optical line emission. Finally, PHL-1811 analogs and WLQs also present relatively strong optical and NUV Fe II emission, as seen in Mrk 231. As discussed in Section 4.2., these similarities between Mrk 231 and “wind-dominated” PHL 1811 analogs and WLQs provide critical new clues on the inner structure of the AGN in Mrk 231.

#### 4.2. Physical Model – Revisited

In Figures 5 and 6 of Paper I, we presented two simple geometrical models that could explain the main features observed in the 2011 COS data, namely the peculiar Ly $\alpha$  emission, the flat and nearly unpolarized FUV continuum, and the absence of broad absorption features in the FUV despite the presence of a strong optical-NUV FeLoBAL outflow. The main difference between the two pictures was the geometry of the BALR. In the simplest picture, we assumed a spherical geometry for the BALR, while a more physically motivated disk geometry was assumed in the second case. In both pictures, the outflowing BALR was assumed to act as both the partial screen for the continuum emission and the source of the observed blueshifted Ly $\alpha$  emission. In both cases, the source of the FUV continuum was assumed to be an accretion disk on scale of  $\sim \text{few} \times 10^{15}$  cm ( $\lesssim 0.01$  pc).

Here we refine these pictures taking into account the new constraints from our Cycle 21 *HST* data and the similarities we found between Mrk 231 and wind-dominated WLQs (Section 4.1). Another important piece of information that has come to our attention since the publication of Paper I is the detection of strong radio flares in Mrk 231 at 20 GHz (Reynolds et al. 2009; 2013) and, more recently, at 1 and 3 mm (Lindberg et al. 2016). Reynolds et al. (2009, 2013) have argued that these flares have blazar-like characteristics and are therefore associated with highly relativistic ejecta whose self-absorbed synchrotron radio emission is enhanced by strong Doppler boosting (Doppler factor  $\delta \gg 1$ ). This is surprising since Mrk 231 is formally a radio-quiet quasar, and more precisely, a BALQSO in which the radio jets are typically suppressed (although see Becker et al. 1997). Given a time variability brightness temperature of  $T_b = (12.4 \pm 3.5) \times 10^{12}$  K and the need to avoid the inverse Compton catastrophe (Marscher et al. 1979; Ghosh & Punsly 2007), Reynolds et al. (2009, 2013) constrained the jet angle to be less than  $\theta_{\text{max}} = 25.6^{+3.2}_{-2.2}$  from the line of sight. This implies a nearly face-on view of the inner accretion disk, assuming the jet is directed along the rotation axis of the inner disk. In this picture, the pc-scale double radio structure detected in VLBA observations is made of a core component that experiences flares and a steep spectrum secondary component corresponding to a compact radio lobe that is associated with the working surface between the confined jet and dense ISM. Warping of the disk structure on larger scale may be responsible for the apparent discrepancies in orientation of structures on scales  $\gtrsim 100$  pc (e.g., Carilli, Wrobel, & Ulvestad 1998; Downes & Solomon 1998; Klockner, Baan, & Garrett 2003; Davies et al. 2004).

This idea of pole-on BAL outflows is not unique to Mrk 231. Ghosh & Punsly (2007) have used the same time-variable  $T_b$  argument as above to argue that an inordinately large fraction of high- $T_b$  BAL QSOs are LoBALQSOs and therefore fall in this category of pole-on outflows. In a more recent paper, DiPompeo, Brotherton, & De Breuck (2012) have argued that there is a distribution of BAL outflow viewing angles that includes near pole-on, based on radio spectral

index (see also Berrington et al. 2013 for another example of pole-on BALQSO).

This interpretation of the radio flares in Mrk 231 first seems at odds with the rather edge-on view of the disk ( $i \gtrsim 45^\circ$ ) favored in the disk scenario discussed in Paper I (as well as Gallagher et al. 2002) to explain the absence of redshifted Ly $\alpha$  emission (in this scenario, the far-side portion of the dust-free BALR, where Ly $\alpha$  is emitted, was largely obscured by the dusty BALR on the near side). This constraint on the orientation can be relaxed if the opening angle subtended by the outflowing dust-free material is narrower than previously assumed. This is precisely what is expected in a system like Mrk 231, which is experiencing near- or super-Eddington accretion (Section 4.1). When  $L/L_{\text{Edd}} \gtrsim 0.3$ , photon trapping and advection become important and the accretion flow becomes geometrically thick, i.e. characterized by narrow low-density funnels along the rotation axis (e.g., Abramowicz et al. 1988; Ohsuga et al. 2005; Jiang et al. 2014; Sadowski et al. 2013, 2014, 2015; McKinney et al. 2014, 2015; Wang et al. 2014). The strong self-shadowing effects of these so-called “slim disks” lead to strong anisotropy of the radiation field, creating “polar radiation cones” and polar radiation-driven outflows. In systems with spinning supermassive black holes, these sub-relativistic outflows coexist with electromagnetic relativistic jets driven by the Blandford-Znajek effect.

A sketch of the revised disk geometry for Mrk 231 is shown in Figure 8. We warn the readers that this sketch is just meant to be illustrative; it is not accurate in detail. Figure 8 is very similar to that shown in Figure 6 of Paper I, except that the disk structure is now geometrically thicker and viewed more face-on than in Paper I. In this picture, the polar outflow is the source of clouds for the BALR. The BELR is comprised of two physically related components, the extended accretion disk atmosphere and the polar wind (e.g., Murray et al. 1995; Murray & Chiang 1995, 1997; Proga et al. 2000; Chelouche & Netzer 2003; Proga & Kallman 2004; Proga 2007; Proga, Ostriker, & Kurosawa 2008; Richards et al. 2011; Kruczek et al. 2011; Richards 2012; Kashi et al. 2013; Wang et al. 2014). The driving mechanism(s) of the polar wind is intentionally left unspecified: while the previously cited models favor radiation pressure driving, magnetohydrodynamic (MHD) driving cannot be ruled out (e.g., Fukumura et al. 2015 and references therein). The outflowing clouds and filaments labeled “dust-free” in this figure are directly exposed to the beamed X-ray + EUV radiation field emitted in the twin low-density funnels of the slim disk. Clouds further from the rotation axis and labeled “dusty” are less influenced by the polar radiation cone and have proportionally smaller outflow velocities relative to their rotational (virialized) velocities. Finally, gas in the extended accretion disk atmosphere and labeled “disk BELR” is shielded from (most of) the EUV and soft X-ray radiation and shares the largely rotational (virialized) motion of the slim disk material.

Figure 8 assumes that all of the EUV-FUV and soft X-ray radiation is produced in the funnels of the slim disk, while the NUV continuum is produced immediately outside of these funnels and the optical continuum is produced further out in the slim disk. Also, no attempt is made to take into account the (possibly important) effects of dust sublimation near intense NUV sources. So, in reality, the division between dust-free and dusty clouds may not be as simple, and the disk BELR likely lies further from the center than the NUV continuum source (to be consistent with results from reverberation mapping; e.g., Peterson et al. 2004). The outflowing

dusty clouds correspond to the FeLo BALR and are also the source of the observed blueshifted FUV line emission, including Ly $\alpha$ , C III] C II  $\lambda$ 1334, and C IV  $\lambda$ 1548 (the observed Ly $\alpha$  emission from these clouds must be produced near the surfaces of these clouds to avoid destruction by dust grains). In contrast, the disk BELR is the source of most of the optical broad-line emission. The small solid angle subtended by the highly ionized gas exposed to the EUV and X-ray radiation emerging from the narrow funnels of slim disks may explain the general deficit of high-ionization emission and absorption lines in Mrk 231, PHL-1811 analogs and WLQs (Luo et al. 2015).

To explain the blazar-like radio flares of Mrk 231, a relativistic jet must also be present along the rotation axis of the accretion disk, and our line of sight to the disk must be close to that axis ( $\lesssim 26^\circ$ ; Reynolds et al. 2013). The compact radio lobe located within  $\sim 1$  pc from the primary radio component is not shown in Figure 8 for clarity. On the other hand, the weakness of the observed FUV and X-ray continua and deduced EUV continuum (from the faint high-ionization lines) strongly argues against a direct view of the beamed ionizing radiation emerging from the twin funnels of the slim disk (e.g., Costelló-Mor, Netzer, & Kaspi 2016). This puts a lower bound on the angle of our line of sight to the rotation axis of order  $\gtrsim 10^\circ$ , although this number depends on the spin of the supermassive black hole and also on the exact structure of the slim disk, which is model-dependent (e.g., Jiang et al. 2014; Sadowski et al. 2013, 2014, 2015; McKinney et al. 2014, 2015).

In this picture, the outflowing dusty BALR acts as a partial screen for the FUV-NUV-optical continuum and BELR emission. A covering fraction of  $\sim 90\%$  was estimated in Rupke et al. (2002) and Paper I based on the non-zero flux in the core of the saturated boxcar profile of Na I D measured from the high-resolution Keck spectrum. Given the similar physical conditions leading to Na I (ionization potential of 5.1 eV) and Mg I (7.6 eV) absorption, one can infer that the NUV absorbers also partially cover the continuum source (although the low spectral resolution of the STIS data does not allow us to directly estimate the covering fraction in the NUV). The profiles of the unblended absorption features (Mg I, He I, Ca II H, and Ca II K) are distinctly narrower than those of the FUV emission lines. In this picture (Fig. 8), the widths of these absorption features reflect the range of velocities of the BALR clouds along our line of sight to the optical-NUV source, while the broader profiles of the FUV emission lines reflect the velocities of all BALR clouds in front of the disk, including the many clouds that are not directly along our line of sight to the optical-NUV source. The absence of redshifted Ly $\alpha$ , C III] and C IV emission is due to obscuration of the disk BELR by the near-side dusty BALR clouds. The fact that the bulk of the BALR clouds cluster around velocities  $\sim [-5500, -3500]$  km s $^{-1}$  suggests that the BALR screen is kinematically detached from the continuum source and does not extend over a broad range of distance from the disk.

The patchy BALR is opaque to the FUV but not to the optical-NUV continuum, consistent with the smaller extinction and polarization in the FUV than in the NUV reported in Paper I and Smith et al. (1995), respectively. The apparently smaller extinction towards the optical / near-infrared continuum relative to the NUV continuum (Leighly et al. 2014) could also be explained in this scenario if the source of the optical / near-infrared continuum emission (e.g., emission from the accretion disk and/or host galaxy) is more extended / less

affected by the dusty BALR than the NUV continuum region. This near face-on view of the accretion disk is also consistent with the relatively small column density recently derived from the *Chandra* + *NuSTAR* data ( $N_H \sim 1 \times 10^{23}$  cm $^{-2}$ ; Teng et al. 2014), as it avoids the highly Compton thick material in the slim disk. In this picture, about 10% of the FUV emission makes it through the BALR, perhaps along the near-side funnel (line of sight #1 in Figure 8).

The observed wild variations in the X-ray and radio (mm- and cm-wave) bands but lack of NUV and FUV continuum and line variability over time scales of up to 22 years provide additional constraints on the structure and duty cycle of this AGN. While the radio variability is attributed to strong Doppler boosting of self-absorbed synchrotron emission from a large injection of relativistic particles (Reynolds et al. 2009, 2013), the X-ray variations are best modeled by changes in absorbing column densities and/or covering factor of the absorbing screen in front of the disk funnel (e.g., Piconcelli et al. 2013; Teng et al. 2014). The disk disruption / jet ejection model used to explain the anti-correlation between radio and X-ray emission in some jetted AGN (e.g., 3C 120; Lohfink et al. 2013) therefore may not apply to Mrk 231. The stability of the FUV-NUV continuum emission and NUV absorption troughs argue in favor of a thick and uniform BALR screen made of numerous clouds and filaments (cf. McGraw et al. 2015).

While a full analysis of the NUV BAL features (see Figures 2 – 3) is not possible here given the poor spectral resolution of the STIS data, some general statements can be made about the properties of the BALR. The BAL features of the ground-state resonant lines Mg II, Mg I, and Na I are strong and relatively simple. Given that Mg I and Na I are easily ionized, their detections in Mrk 231 imply that there is very high density and well-shielded gas consistent with our picture of dust in the outflow. Fe II from various excited states (UV60, 61, 62, 63, and 78) are also clearly present in the STIS spectrum, as is often the case in other FeLoBAL outflows (e.g., Hall et al. 2002). Conclusions drawn from the detailed analyses of some of these other FeLoBALs may thus also apply to the outflow in Mrk 231.

The detection of He I\*  $\lambda$ 3889 requires  $\log N_H$  (cm $^{-2}$ )  $\gtrsim 22.5$  and large ionization parameters in an *ionized* He II / H II absorbing region (e.g., Leighly et al. 2011; Hamann et al. 2016, in prep.). Large columns are needed because this line arises from the metastable  $2s\ ^3S$  state that is 19.8 eV above ground state. Fe II, Ca II, Mg I, and Na I require an additional separate column of warm neutral gas, nominally behind the ionized He II / H II zone. However, Ca II and Na I (5.1 eV corresponding to  $\sim 2400$  Å) are not radiatively shielded behind the H II – H I recombination front. Dust appears to be required to provide this shielding in at least the Na I absorbing region. Hamann et al. (2016, in prep.) discuss the physical conditions needed for Na I and other low-ionization lines in the context of another outflow quasar with many FeLoBAL-like features. Those results suggest that the Na I lines in Mrk 231 require a neutral column with  $\log N_H$  (cm $^{-2}$ )  $\sim 22 - 22.5$  and enough dust to provide extinction equivalent to  $A_V \sim 1 - 2$  mag.

The Fe II UV60, 61, 62, 63, and 78 lines arise from an excited state at  $\sim 1.0$  eV, which requires  $n_H \gtrsim 10^5$  cm $^{-3}$  to populate these levels and produce the lines we observe in Mrk 231 (Hamann et al. 2016, in prep.). This is not a strong constraint, but if we assume that this limit applies also to the ionized gas producing He I\*  $\lambda$ 3889, then the combination of a minimum



density and minimum ionization parameter ( $\log U \geq -1$ ) lead to a distance  $\lesssim 2 - 20$  pc between the absorber and the ionizing continuum source. For this calculation, we used equation (A1) from Hamann et al. (2011) that relates  $n_H$ ,  $U$ , and  $\nu L_\nu(1450)$ , the luminosity at  $1450 \text{ \AA}$  as seen by the BAL clouds, and assumed  $\nu L_\nu(1450) = 0.6 - 90 \times 10^{43} \text{ erg s}^{-1}$  corresponding to extinctions  $A_V \sim 0 - 1$  mag. to our line of sight for Galactic, LMC, or SMC extinction curves. This distance falls slightly below the range of distances ( $13 - 230$  pc) derived by Leighly et al. (2014) using photoionization models to reproduce  $\text{Ly}\alpha$ ,  $\text{He I}^*$  3889 and 10830,  $\text{Ca II H}$  and  $\text{K}$ ,  $\text{Na I D}$ , and  $\text{Fe II}$ . The mass outflow rate and kinetic luminosity of the BAL outflow derived in that paper therefore need to be proportionally scaled down to  $\lesssim 10 - 100 M_\odot \text{ yr}^{-1}$  and  $\lesssim 10^{44-45} \text{ erg s}^{-1}$  to account for the smaller distance of the absorbers inferred from the detection of  $\text{Fe II}$  from excited states.

#### 4.3. Evidence against the Binary Black Hole Model of Yan et al. (2005)

An alternative model has recently been proposed by Yan et al. (2015) to explain the peculiar optical-to-UV SED of Mrk 231: continuum emission from accretion flows onto a tight binary black hole, with a semimajor axis of  $\sim 590$  AU and an orbital period  $t_{\text{orb}} \sim 1.2$  yrs. In their model, the optical continuum is produced by a circumbinary disk, while the FUV continuum is produced by a mini-disk surrounding the secondary black hole. The sharp drop-off observed at  $2500 - 4000 \text{ \AA}$  is interpreted as a flux deficit due to a gap (or hole) opened by the secondary black hole migrating within the circumbinary disk. Given the morphological evidence that Mrk 231 is indeed a recent merger (e.g., Hamilton & Keel 1987; Hutchings & Neff 1987; Surace et al. 1998; Veilleux et al. 2002, 2006), and the dearth so far of black hole binaries in the cores of quasars (e.g., Popović 2012; Eracleous et al. 2012; Shen et al. 2013; Liu et al. 2014; Runnoe et al. 2015), contrary to theoretical expectations (Begelman et al. 1980; Yu 2002; Merritt & Milosavljević 2005), the binary black hole explanation for the peculiar SED of Mrk 231 is potentially a very exciting new explanation of the Cycle 19 data, so it deserves to be examined in detail taking into account the new constraints from the Cycle 21 data.

As pointed out by Yan et al. (2015), numerical simulations of black hole binaries (e.g., Miller & Krolik 2013; Farris et al. 2014ab; Roedig et al. 2014) show that the accretion onto the secondary black hole is expected to vary on a timescale of the order of the black hole binary orbital period,  $t_{\text{orb}} \sim 1.2$  years, or less. However, as described here and in Paper I, the UV continuum emission in Mrk 231 has been surprisingly constant over the last several years. There is no evidence for any flux variations in the FUV continuum emission between 2011 (Paper I) and 2014 (this paper), or  $\sim 3 \times t_{\text{orb}}$ , and in the NUV continuum emission between 1992 (Smith et al. 1995) and 2014 (this paper), or  $\sim 18 \times t_{\text{orb}}$ . This is not to say that the UV continuum of Mrk 231 does not vary at all. In fact, there is some evidence that the continuum level near  $1300 \text{ \AA}$  in the 1978 archival *International Ultraviolet Explorer* (IUE) spectra of Mrk 231 (published in Hutchings & Neff 1987) was  $\sim 1.5 \times$  higher than the continuum level measured in our recent COS FUV data. But, the binary black hole model has difficulties explaining the stability of the UV emission in recent years. It would imply a (unrealistically) steady accretion stream of gas from the inner edge of the circumnuclear binary

to the mini-disk of the secondary black hole over timescales of  $\sim 3 - 18 t_{\text{orb}}$ .

A potentially fatal hurdle of the binary black hole model is the stability of the  $\text{Ly}\alpha$  profile over a period of  $\sim 3$  yrs ( $\sim 3 \times t_{\text{orb}}$ ). In this model, the mini-disk of the secondary black hole is expected to dominate the line emission in the FUV, and the large blueshift of  $\text{Ly}\alpha$ , C III], and C IV would therefore be due to the expected large line-of-sight velocity of the secondary black hole as it orbits the primary black hole. However, if this were the case, one would expect the centroid of the  $\text{Ly}\alpha$  profile to shift in velocity from  $-3000$  to at least  $+3000 \text{ km s}^{-1}$  over half an orbital period. This is firmly ruled out by the new Cycle 21 data.

Another difficulty with the binary black hole model is the fact that the absorption lines are only observed in the NUV and optical, but not in the FUV. This means that the BALR must be present in the direction of the optical/NUV continuum source, the circumbinary disk, but not in the direction of the FUV continuum source, the mini-disk of the secondary black hole. This seems hard to explain without invoking a contrived geometry of the BALR. Moreover, one would naively expect the velocities of the FUV emission lines to be significantly different from the velocities of the NUV/optical absorption lines, but this is not the case (Figure 7). Recently, Leighly et al. (2016) has also argued that the binary black hole model has difficulties explaining the strong broad near-infrared recombination line emission relative to the C IV line emission.

Finally, it is worth repeating that the spectropolarimetric study of Smith et al. (1995) find that the polarization level peaks at a value of  $\sim 15\%$  around  $3100 \text{ \AA}$ , decreasing in the UV from  $\sim 3100$  to  $1600 \text{ \AA}$ , becoming essentially zero at the shortest wavelengths. The polarization also monotonically decreases from  $\sim 3100$  to  $\sim 7600 \text{ \AA}$ . This latter trend with wavelength cannot be explained via polarization from electron scattering off of an asymmetric structure (e.g., edge of circumbinary disk; Yan et al. 2015). Smith et al. (1995) argue that this trend is due to the frequency-dependent scattering cross-section of dust grains, while the trend in the UV has been explained in the past as dilution by either unobscured/unpolarized starlight (Smith et al. 1995; Leighly et al. 2014) or AGN emission (Paper I and this paper). In the binary black hole scenario, these spectropolarimetric results would again seem to imply a contrived geometry of the dust distribution with respect to the black hole binary, where the small-disk FUV emission is somehow unobscured/unpolarized while the NUV-optical emission from the larger circumbinary disk is obscured/polarized.

## 5. SUMMARY

We report the results of our analysis of new far- and near-ultraviolet ( $\sim 1150 - 3000 \text{ \AA}$ ) spectra of Mrk 231 obtained with *HST* COS and STIS in Cycle 21 (2014), as well as a near-contemporaneous optical spectrum obtained with the 4.3-meter DCT. These data are compared with our Cycle 19 (2011) COS FUV ( $\sim 1150 - 1470 \text{ \AA}$ ) spectra published in Paper I and archival NUV data. The main results of this analysis are:

- The  $\text{Ly}\alpha$  and  $\text{H}\alpha$  emission profiles and optical and FUV continuum emission have not varied significantly over the past  $\sim 3$  years. The  $\text{Ly}\alpha$  emission is faint, broad ( $\gtrsim 10,000 \text{ km s}^{-1}$  at the base), and highly blueshifted

(centroid at  $\sim -3000 \text{ km s}^{-1}$ ), while  $\text{H}\alpha$  is strong and highly symmetric, spanning a range in velocity that is at least as large as that of  $\text{Ly}\alpha$ . The FUV continuum is featureless (i.e. no obvious absorption features of stellar or AGN origin) and nearly flat.

- The broader wavelength coverage of the new data now reveals that the FUV C III]  $\lambda 1909$  and C IV  $\lambda 1548$  emission features have line profiles that resemble that of  $\text{Ly}\alpha$ , while the profiles of the NUV He I, Mg I, Mg II, and Fe II absorption features resemble that of the optical Na I D, He I\*  $\lambda 3889$ , and Ca II H and K lines, exhibiting broad blueshifted troughs that overlap in velocity space with the FUV emission-line features. The sharp upturn of the NUV-optical continuum emission above  $\sim 2400 \text{ \AA}$ , noted in Paper I and other papers but based only on archival data taken at different epochs, is also seen in the new near-contemporaneous data. A comparison with the 1992 *HST* FOS data of Smith et al. (1995) shows no evidence for changes in the NUV continuum emission and absorption features over the past 22 years. Multiple lines of evidence indicate that the NUV emission is unresolved on scale  $\lesssim 40 \text{ pc}$ . The flux of the STIS and COS data are consistent with each other in the overlap region, implying a FUV continuum-emitting size  $\lesssim 170 \text{ pc}$  and again favoring an AGN origin for the FUV emission rather than a stellar origin.
- These results strengthen the conclusions from Paper I that the NUV – FUV continuum emission is produced predominantly by the AGN rather than stellar processes. The FUV continuum emission is partially ( $\sim 90\%$ ) blocked but otherwise unaffected by the dusty FeLoBAL screen, while the NUV continuum emission is filtered by this screen. The observed FUV line emission appears to be produced in the outflowing BAL cloud system, while the Balmer lines arise primarily from the standard broad emission line region seen through the dusty FeLoBAL.
- The BAL detections in ground and excited states of Fe II and He I as well as in Na I, Mg I, Mg II and Ca II require densities  $\gtrsim 10^5 \text{ cm}^{-3}$ , ionization parameters  $\log U \geq -1.0$ , ionized gas column densities  $\log N_H (\text{cm}^{-2}) \gtrsim 22.5$ , neutral gas column densities  $\log N_H (\text{cm}^{-2}) \sim 22 - 22.5$ , and enough dust to provide extinction equivalent to at least  $A_V \sim 1 - 2 \text{ mag}$ . The lower limits on the density and ionization parameter imply a distance for the FeLoBAL screen of  $\lesssim 2 - 20 \text{ pc}$  from the ionizing source. The inferred mass outflow rate and kinematic luminosity of the BAL outflow is  $\lesssim 10 - 100 M_\odot \text{ yr}^{-1}$  and  $\lesssim 10^{44-45} \text{ erg s}^{-1}$ , respectively.
- We revise the geometrical disk model discussed in Paper I, taking into account the constraints from our new data and the recent detection of blazar-like radio flares in Mrk 231. We draw an analogy with weak-lined “wind-dominated” quasars which share many of the peculiar UV and X-ray spectroscopic properties of Mrk 231, and have similar high (often super-Eddington) accretion rates. We favor a picture where the inner accretion structure of Mrk 231 is geometrically thick with twin narrow funnels that drive

(radiation- or MHD-driven) polar winds, coexistent with electromagnetic relativistic jets. Our view of this “slim disk” must be nearly face-on to explain the high-frequency radio data. We associate the dust-free outflowing clouds in this picture with the absorbing material in the X-rays. The outflowing dusty clouds correspond to the FeLoBAL screen seen in the NUV-optical and are also the source of the observed blueshifted FUV line emission. In contrast, the extended accretion disk atmosphere is the source of most of the optical broad-line emission.

- The results of our analysis of these new data and comparisons with the older data are inconsistent with the predictions of the tight sub-pc binary AGN scenario proposed by Yan et al. (2015). The lack of FUV emission variability imply unrealistically steady accretion stream of gas from the inner edge of the circumnuclear binary to the mini-disk of the secondary black hole. One would also expect the orbital motion of the secondary component around the primary to produce large velocity shifts in the  $\text{Ly}\alpha$  emission profile over the orbital period  $t_{\text{orb}} \sim 1.2 \text{ yr}$ , but these shifts are not observed. The near-zero polarization and absence of BALs in the FUV, while the optical/NUV spectrum shows strong BALs and substantial polarization, would imply a very contrived geometry of the dusty FeLoBAL screen. The good match in velocities of the optical/NUV absorption lines and FUV emission lines seems inconsistent with this picture, regardless of the exact geometry.

Our results suggest that Mrk 231 is the nearest example of “wind-dominated” high accretion rate weak-lined quasars. Super-critical black hole accretion is potentially relevant to a broad range of phenomena including ultraluminous X-ray sources (ULX), tidal disruption events (TDEs), and hyper-accreting supermassive black holes at high redshifts. However, the fractions of PHL-1811 analogs and WLQs among typical quasars are small,  $1\% - 2\%$  (Wu et al. 2011). It is not clear why that is the case. Figure 8 suggests that orientation effects may play a role (e.g., a more edge-on view of Mrk 231 might obscure the fast wind). Another possibility is that the conditions needed to reach near- or super-Eddington accretion rates are generally not present in local quasars, except perhaps in some rare luminous gas-rich merger events as in Mrk 231 (although see Du et al. 2016 for other exceptions). In this context, Mrk 231 offers a unique local laboratory to study a phenomenon that might be fundamental to our understanding of the creation of supermassive black holes in the early universe.

S.V. acknowledges useful discussions regarding the high-frequency radio data of Mrk 231 with Drs. B. Punsly and C. Reynolds. We thank J. I. Capone and Dr. S. B. Cenko for obtaining the 2015 DCT optical spectrum and reducing it, respectively. We also thank the anonymous referee for useful suggestions that have improved this paper. Support for this work was provided to S.V. and M.M. by NASA through contract *HST* GO-13460.001-A. S.V. also acknowledges support from the National Science Foundation through grant AST-1207785. This work made use of the Discovery Channel Telescope at Lowell Observatory. Lowell is a private, non-profit institution dedicated to astrophysical research and pub-



lic appreciation of astronomy and operates the DCT in partnership with Boston University, the University of Maryland, the University of Toledo and Northern Arizona University. It also made use of NASA's Astrophysics Data System Abstract

Service and the NASA/IPAC Extragalactic Database (NED), which is operated by the Jet Propulsion Laboratory, California Institute of Technology, under contract with the National Aeronautics and Space Administration.

## REFERENCES

- Aalto, S., et al. 2012, *A&A*, 537, 44  
 Alatalo, K. 2015, *ApJ*, 801, L17  
 Allen, J. T., et al. 2011, *MNRAS*, 410, 860  
 Armus, L., et al. 2007, *ApJ*, 656, 148  
 Baldwin, J. A., et al. 1996, *ApJ*, 461, 664  
 Bautista, M., et al. 2010, *ApJ*, 713, 25  
 Becker, R. H., et al. 1997, *ApJ*, 479, L93  
 Begelman, M. C., Blandford, R. D., & Rees, M. J. 1980, *Nature*, 287, 307  
 Berrington, R. C., Brotherton, M. S., Gallagher, S. C., Ganguly, R., Shang, Z., et al. 2013, *MNRAS*, 436, 3321  
 Blackburne, J. A., et al. 2011, *ApJ*, 729, 34  
 Boksenberg, A., et al. 1977, *MNRAS*, 178, 451  
 Boroson, T. A., et al. 1991, *ApJ*, 370, L19  
 Braito, V., et al. 2004, *A&A*, 420, 79  
 Brusa, M., et al. 2016, *A&A*, 588, 58  
 Carilli, C. L., Wrobel, J. M., & Ulvestad, J. S. 1998, *AJ*, 115, 928  
 Chelouche, D., & Netzer, H. 2003, *MNRAS*, 344, 233  
 Cicone, C., Feruglio, C., Maiolino, R., Fiore, F., Piconcelli, E., et al. 2012, *A&A*, 543, 99  
 Cicone, C., Maiolino, R., Sturm, E., Graciá-Carpio, J., Feruglio, C., et al. 2014, *A&A*, 562, 21  
 Cicone, C., Maiolino, R., Gallerani, S., Neri, R., Ferrara, A., et al. 2015, *A&A*, 574, 14  
 Conroy, C., et al. 2010, *ApJ*, 718, 184  
 Castelló-Mor, N., Netzer, H., & Kaspi, S. 2016, *MNRAS*, 458, 1839  
 Cresci, G., et al. 2015, *ApJ*, 799, 82  
 Croton, D. J., Springel, V., White, S. D. M., De Lucia, G., Frenk, C. S., et al. 2006, *MNRAS*, 365, 11  
 Davies, R. I., Tacconi, L. J., & Genzel, R. 2004, *ApJ*, 613, 781  
 Davis, S. W., Woo, J.-H., & Blaes, O. M. 2007, *ApJ*, 668, 682  
 Di Matteo, T., Springel, V., & Hernquist, L. 2005, *Nature*, 433, 604  
 DiPompeo, M. A., Brotherton, M. S., & De Breuck, C. 2012, *ApJ*, 752, 6  
 Downes, D., & Solomon, P. M. 1998, *ApJ*, 507, 615  
 Du, P., et al. 2016, *ApJ*, 820, 27  
 Edmonds, D., et al. 2011, *ApJ*, 739, 7  
 Elvis, M. 2000, *ApJ*, 545, 63  
 Eracleous, M., et al. 2012, *ApJS*, 201, 23  
 Fall, S. M., Pei, Y. C., & McMahon, R. G. 1989, *ApJ*, 341, L5  
 Farris, B. D., Duffell, P., MacFadyen, A. I., & Haiman, Z. 2014a, *ApJ*, 783, 134  
 Farris, B. D., Duffell, P., MacFadyen, A. I., & Haiman, Z. 2014b, *MNRAS*, 446, L36  
 Faucher-Giguère, C.-A., & Quataert, E. 2012, *MNRAS*, 425, 605  
 Faucher-Giguère, C.-A., Quataert, E., & Murray, N. 2012, *MNRAS*, 420, 1347  
 Feruglio, C., et al. 2010, *A&A*, 518, L155  
 Feruglio, C., et al. 2015, *A&A*, 583, A99  
 Fischer, J., et al. 2010, *A&A*, 518, L41  
 Forster, K., Rich, R. M., & McCarthy, J. K. 1995, *ApJ*, 450, 74  
 Fukumura, K., Tombesi, F., Kazanas, D., Shrader, C., Behar, E., & Contopoulos, I. 2015, *ApJ*, 805, 17  
 Gallagher, S. C., et al. 2002, *ApJ*, 569, 655  
 Gallagher, S. C., et al. 2005, *ApJ*, 633, 71  
 Ghavanian, P., et al. 2010, in the Proceedings of the “2010 Space Telescope Science Institute Workshop – Hubble after SM4”, ed. S. Deustua and C. Oliveira, p. 46  
 Ghosh, K. K., & Punnsly, B. 2007, *ApJ*, 661, L139  
 Gibson, R. R., et al. 2008, *ApJ*, 675, 985  
 Gibson, R. R., et al. 2009, *ApJ*, 692, 758  
 Glikman, E., et al. 2012, *ApJ*, 757, 51  
 Goobar, A. 2008, *ApJ*, 686, L103  
 Goodrich, R. W., & Miller, J. S. 1994, *ApJ*, 434, 82  
 Green, J. C., et al. 2012, *ApJ*, 744, 60  
 Hall, P. B., et al. 2002, *ApJS*, 141, 267  
 Hall, P. B., et al. 2004, *Multiwavelength AGN Surveys*, ed. R. Mujica and R. Maiolino, 247  
 Hall, P. B., et al. 2011, *MNRAS*, 411, 2653  
 Hamann, F., Korista, K. T., & Morris, S. L. 1993, *ApJ*, 415, 541  
 Hamann, F., & Sabra, B. 2004, in *AGN Physics with the Sloan Digital Sky Survey*, ASP Conf. Series, 311, p. 203  
 Hamilton, D., & Keel, W. C. 1987, *ApJ*, 321, 211  
 Hartig, G. F., & Baldwin, J. A. 1986, *ApJ*, 302, 64  
 Hopkins, P. F., Cox, T. J., Kereš, D., & Hernquist, L. 2008, *ApJS*, 175, 390  
 Hutchings, J. B., & Neff, S. G. 1987, *AJ*, 92, 14  
 James, B. L., Aloisi, A., Heckman, T., Sohn, S. T., & Wolfe, M. A. 2014, *ApJ*, 795, 109  
 Jiang, Y.-F., Stone, J. M., & Davies, S. W. 2014, *ApJ*, 796, 106  
 Kashi, A., Proga, D., Nagamine, K., Greene, J., & Barth, A. J. 2013, *ApJ*, 778, 50  
 Kawakatu, N., Imanishi, M., & Nagao, T. 2007, *ApJ*, 661, 660  
 Keeney, B. A., et al. 2012, *PASP*, 124, 830  
 Klockner, H.-R., Baan, W. A., & Garrett, M. A. 2003, *Nature*, 421, 821  
 Kollatschny, W., Dietrich, M., & Hagen, H. 1992, *A&A*, 264, L5  
 Kramer, R. H., & Haiman, Z. 2009, *MNRAS*, 400, 1493  
 Krolik, J. H., & McKee, C. F. 1978, *ApJS*, 37, 459  
 Kruczek, N. E., et al. 2011, *AJ*, 142, 130  
 Krug, H. B., Rupke, D. S. N., & Veilleux, S. 2010, *ApJ*, 708, 1145  
 Laor, A., et al. 1997, *ApJ*, 489, 656  
 Lau, M. W., Prochaska, J. X., & Hennawi, J. F. 2015, preprint (arXiv:1510.06018v2)  
 Leighly, K. M., Dietrich, M., & Barber, S. 2011, *ApJ*, 728, 94  
 Leighly, K., Halpern, J. P., Jenkins, E. B., et al. 2007a, *ApJ*, 663, 103  
 Leighly, K., Halpern, J. P., Jenkins, E. B., Casebeer, D. 2007b, *ApJS*, 173, 1  
 Leighly, K. M., Terndrup, D. M., Baron, E., Lucy, A., Dietrich, M., & Gallagher, S. C. 2014, *ApJ*, 788, 123  
 Leighly, K., Terndrup, D. M., Gallagher, S., & Lucy, A. B. 2016, preprint (arXiv:160403456)  
 Leitherer, C., et al. 2001, *ApJ*, 550, 724  
 Lindberg, J. E., et al. 2016, *A&A*, 587, 15  
 Lipari, S., Colina, L., & Macchetto, F. 1994, *ApJ*, 427, 174  
 Lipari, S., et al. 2009, *MNRAS*, 392, 1295  
 Liu, X., Shen, Y., Bian, F., Loeb, A., & Tremaine, S. 2014, *ApJ*, 789, 140  
 Lohfink, A. M., et al. 2013, *ApJ*, 772, 83  
 Lucy, A. B., Leighly, K. M., Terndrup, D. M., Dietrich, M., & Gallagher, S. C. 2014, *ApJ*, 783, 58  
 Luo, B., et al. 2013, *ApJ*, 772, 153  
 Luo, B., et al. 2015, *ApJ*, 805, 122  
 Maiolino, R., et al. 2012, *MNRAS*, 425, L66  
 Marscher, A., Marshall, F. E., Mushotzky, R. F., et al. 1979, *ApJ*, 233, 498  
 Merritt, D., & Milosavljević, M. 2005, *LRR*, 8, 8  
 McGraw, S. M., et al. 2015, *MNRAS*, 453, 1379  
 McKinney, J. C., Tchekhovskoy, A., & Blandford, R. D. 2012, *MNRAS*, 423, 3083  
 McKinney, J. C., Tchekhovskoy, A., & Blandford, R. D. 2013, *Science*, 339, 49  
 McKinney, J. C., Tchekhovskoy, A., Sadowski, A., & Narayan, R. 2014, *MNRAS*, 441, 3177  
 McKinney, J. C., Dai, L., & Avara, M. J. 2015, *MNRAS*, 454, L6  
 Miller, M. C., & Krolik, J. H. 2013, *ApJ*, 774, 43  
 Morabito, L. K., et al. 2011, *ApJ*, 737, 46  
 Morton, D. C. 2003, *ApJS*, 149, 205  
 Murray, N., & Chiang, J. 1995, *ApJ*, 454, L105  
 Murray, N., & Chiang, J. 1997, *ApJ*, 474, 91  
 Murray, N., Quataert, E., & Thompson, T. A. 2005, *ApJ*, 618, 569  
 Murray, N., et al. 1995, *ApJ*, 451, 498  
 Ohsuga, K., Mori, M., Nakamoto, T., & Mineshige, S. 2005, *ApJ*, 628, 368  
 Peterson, B. M., Ferrarese, L., Gilbert, K. M., Kaspi, S., Malkan, M. A., et al. 2004, *ApJ*, 613, 682  
 Plotkin, R. M., et al. 2015, *ApJ*, 805, 123  
 Popović, L. C. 2012, *NewAR*, 56, 74 2012  
 Prochaska, J. X., Lau, M. W., & Hennawi, J. F. 2014, *ApJ*, 796, 140  
 Proga, D., & Kallman 2004, *ApJ*, 616, 688  
 Proga, D. 2007, *ApJ*, 661, 693  
 Proga, D., Ostriker, J. P., & Kurosawa, R. 2008, *ApJ*, 676, 101  
 Proga, D., Stone, J. M., & Kallman, T. R. 2000, *ApJ*, 543, 686  
 Punnsly, B. 1999a, *ApJ*, 527, 609  
 Punnsly, B. 1999b, *ApJ*, 527, 624  
 Punnsly, B., & Lipari, S. 2005, *ApJ*, 623, L101  
 Reichard, T. A., et al. 2003, *AJ*, 126, 2594  
 Reynolds, C., Punnsly, B., Kharb, P., O'Dea, C. P., & Wrobel, J. 2009, *ApJ*, 706, 851

- Reynolds, C., Punsly, B., O’Dea, C. P., & Hurley-Walker, N. 2013, *ApJ*, 776, L21
- Richards, G. T., et al. 2002, *AJ*, 124, 1
- Richards, G. T., et al. 2011, *ApJ*, 141, 167
- Richards, G. T. 2012, in “AGN Winds in Charleston”, preprint (arXiv:1201.2595)
- Robert, C., et al. 2003, *ApJS*, 144, 21
- Roedig, C., Krolik, J. H., & Miller, M. C. 2014, *ApJ*, 785, 115
- Rubin, K. H. R., Prochaska, J. X., Koss, D. C., Phillips, A. C., Martin, C. L., & Winstrom, L. O. 2014, *ApJ*, 794, 156
- Rubin, K. H. R., Hennawi, J. F., Prochaska, J. X., Simcoe, R. A., Myers, A., & Lau, M. W. 2015, *ApJ*, 808, 38
- Rudy, R. J., Foltz, C. B., & Stocke, J. T. 1985, *ApJ*, 288, 531
- Runnoe, J. C., et al. 2015, *ApJS*, 221, 7
- Rupke, D. S. N., & Veilleux, S. 2011, *ApJ*, 729, L27
- Rupke, D. S. N., & Veilleux, S. 2013, *ApJ*, 768, 75
- Rupke, D. S., Veilleux, S., & Sanders, D. B. 2002, *ApJ*, 570, 588
- Rupke, D. S., Veilleux, S., & Sanders, D. B. 2005, *ApJ*, 632, 751
- Sadowski, A., Narayan, R., Penna, R., & Zhu, Y. 2013, *MNRAS*, 436, 3856
- Sadowski, A., Narayan, R., McKinney, J. C., & Tchekhovskoy, A. 2014, *MNRAS*, 439, 503
- Sadowski, A., Narayan, R., Tchekhovskoy, A., Abarca, D., Zhu, Y., & McKinney, J. C. 2015, *MNRAS*, 447, 49
- Sadowski, A., & Narayan, R. 2015a, *MNRAS*, 453, 3213
- Sanders, D. B., & Mirabel, I. F. 1996, *ARA*, 34, 749
- Sanders, D. B., et al. 1988, *ApJ*, 325, 74
- Schaerer, D., et al. 2011, *A&A*, 531, 12
- Schmidt, G. D., & Miller, J. S. 1985, *ApJ*, 290, 517
- Shen, Y., Liu, X., Loeb, A., & Tremaine, S. 2013, *ApJ*, 775, 49
- Smith, P. S. et al. 1995, *ApJ*, 444, 146
- Smith, J. E. et al. 2004, *MNRAS*, 350, 140
- Spoon, H. W. W., Farrah, D., Leboutteiller, V., González-Alfonso, E., Bernard-Salas, J., et al. 2013, *ApJ*, 775, 127
- Sturm, E., et al. 2011, *ApJ*, 733, L16
- Surace, J., et al. 1998, *ApJ*, 492, 116
- Teng, S. H., Brandt, W. N., Harrison, F. A., et al. 2014, *ApJ*, 785, 19
- Thompson, I., et al. 1980, *MNRAS*, 192, 53
- Tripp, T. M., Meiring, J. D., Prochaska, J. X., Willmer, C. N. A., Howk, J. C., et al. 2011, *Science*, 334, 952
- Trump, J. R. et al. 2006, *ApJS*, 165, 1.
- Tumlinson, J., Thom, C., Werk, J. K., Prochaska, J. X., Tripp, T. M., et al. 2011, *Science*, 334, 948
- Ulvestad, J., Wrobel, J. M., & Carilli, C. L. 1999, *ApJ*, 516, 127
- Urrutia, T., et al. 2009, *ApJ*, 698, 1095
- vanden Berk, D. E., et al. 2001, *AJ*, 122, 549
- Vázquez, G., et al. 2004, *ApJ*, 600, 162
- Veilleux, S. 2012, *Journal of Physics, Conf. Series* Vol. #372, 012001
- Veilleux, S., Cecil, G., & Bland-Hawthorn, J. 2005, *ARA&A*, 43, 769
- Veilleux, S., Kim, D.-C., & Sanders, D. B. 2002, *ApJS*, 143, 315
- Veilleux, S., et al. 2006, *ApJ*, 643, 707
- Veilleux, S., et al. 2009, *ApJS*, 182, 628
- Veilleux, S., Teng, S. H., Rupke, D. S. N., Maiolino, R., & Sturm, E. 2014, *ApJ*
- Veilleux, S., Trippe, M., Hamann, F., et al. 2013a, *ApJ*, 764, 15 (Paper I)
- Veilleux, S., Meléndez, M., Sturm, E., et al. 2013b, *ApJ*, 776, 27
- Verhamme, A., Schaerer, D., & Maselli, A. 2006, *A&A*, 460, 397
- Wang, J.-M., Qiu, J., Du, P., & Ho, L. C. 2014, *ApJ*, 797, 65
- Werk, J. K., Prochaska, J. X., Tumlinson, J., Peebles, M. S., Tripp, T. M., et al. 2014, *ApJ*, 792, 8
- Werk, J. K., Prochaska, J. X., Thom, C., Tumlinson, J., Tripp, T. M., O’Meara, J. M., & Peebles, M. S. 2013, *ApJS*, 204, 17
- Wu, J. et al. 2011, *ApJ*, 736, 28
- Wu, J. et al. 2012, *ApJ*, 747, 10
- Yan, C.-S., Lu, Y., Dai, X., & Yu, Q. 2015, *ApJ*, 809, 117
- Yu, Q. 2002, *MNRAS*, 331, 935
- Zakamska, N. L., & Greene, J. E. 2014, *MNRAS*, 442, 784
- Zakamska, N. L., Hamann, F., Paris, I., Brandt, W. N., Greene, J.E., et al. 2015, preprint (arXiv:151202642)
- Zakamska, N. L., et al. 2016, *MNRAS*, 455, 4191
- Zheng, W., et al. 1997, *ApJ*, 475, 469

TABLE 1  
STRONGEST UV AND OPTICAL SPECTRAL FEATURES IN MRK 231

Line ID (1)	Flux (2)	REW (3)	$f_\lambda$ (4)	$V_{50}$ (5)	$V_{84}$ (6)	$V_{98}$ (7)
Ly $\alpha$ $\lambda$ 1215.67	+78	-71	1.1	-2771	-5179	-7071
Ly $\alpha$ $\lambda$ 1215.67 (COS 2011)	+74	-68	1.1	-2739	-5167	-7039
C II $\lambda$ 1334.43	+13	-11	1.2	-3232	-4565	-6143
C IV $\lambda$ 1548.20	+16	-12	1.3	-3253	-4910	-6003
C III] $\lambda$ 1909.0	+15	-14	1.0	-3636	-5903	-7072
Fe II UV2 $\lambda$ 2382 <sup>a</sup>	-21	+14	1.5	-3810	-5865	-7121
Fe II UV1 $\lambda$ 2599 <sup>a</sup>	-59	+26	2.2	-3907	-6155	-7407
Fe II UV62/63 $\lambda$ 2739 <sup>a</sup>	-32	+12	2.7	-3521	-5664	-6610
Mg II $\lambda$ 2796.3, 2803.4	-36	+12	3.0	-4742	-5572	-6191
Mg I $\lambda$ 2853.0	-23	+6.5	3.6	-4620	-4997	-5317
He I $\lambda$ 2945.11	-19.8	+4.7	4.2	-4143	-5018	-5814
He I* $\lambda$ 3888.65 (Keck 2001)	-58.9	+7.1	8.3	-4565	-4967	-6068
Ca II K $\lambda$ 3933.66 (Keck 2001)	-56.1	+6.3	8.9	-4498	-4775	-5059
Ca II H $\lambda$ 3968.47 (Keck 2001)	-41.6	+4.6	9.0	-4491	-4699	-4985
Na I D $\lambda$ 5890, 5896 (DCT 2015)	-124	+20	6.2	-4573	-5105	-6225
Na I D $\lambda$ 5890, 5896 (Keck 2001)	-126	+21	6.0	-4451	-5005	-6639
H $\alpha$ $\lambda$ 6562.80 (DCT 2015)	+1579	-266	5.9	-321	-2727	-6620
H $\alpha$ $\lambda$ 6562.80 (Keck 2001)	+1414	-255	5.5	-33	-2325	-6087

NOTE. — All measurements refer to the Cycle 21 2014 COS and STIS data unless otherwise noted. Col. (1): Line ID and rest-frame wavelength of the feature in  $\text{\AA}$  used for the calculations of the velocities. In the cases of the multiplets (labeled as <sup>a</sup>), the velocities are calculated with respect to the ground-state resonant transition. Col. (2): Flux of the feature in  $10^{-15} \text{ erg s}^{-1} \text{ cm}^{-2}$  (positive value corresponds to emission). Col. (3): Rest-frame equivalent width of the feature in  $\text{\AA}$  (negative value corresponds to emission). Col. (4): Continuum level at the position of the feature in  $10^{-15} \text{ erg s}^{-1} \text{ cm}^{-2} \text{ \AA}^{-1}$ . Col. (5): 50-percentile (centroid) velocity in  $\text{km s}^{-1}$ , a measure of the bulk velocity of the outflow, if present. Col. (6): 84-percentile velocity in  $\text{km s}^{-1}$ , corresponding to  $1 \sigma$  blueward of the centroid velocity. Col. (7): 98-percentile velocity in  $\text{km s}^{-1}$ , corresponding to  $2 \sigma$  blueward of the centroid velocity, a measure of the maximum velocity of the outflow, if present.



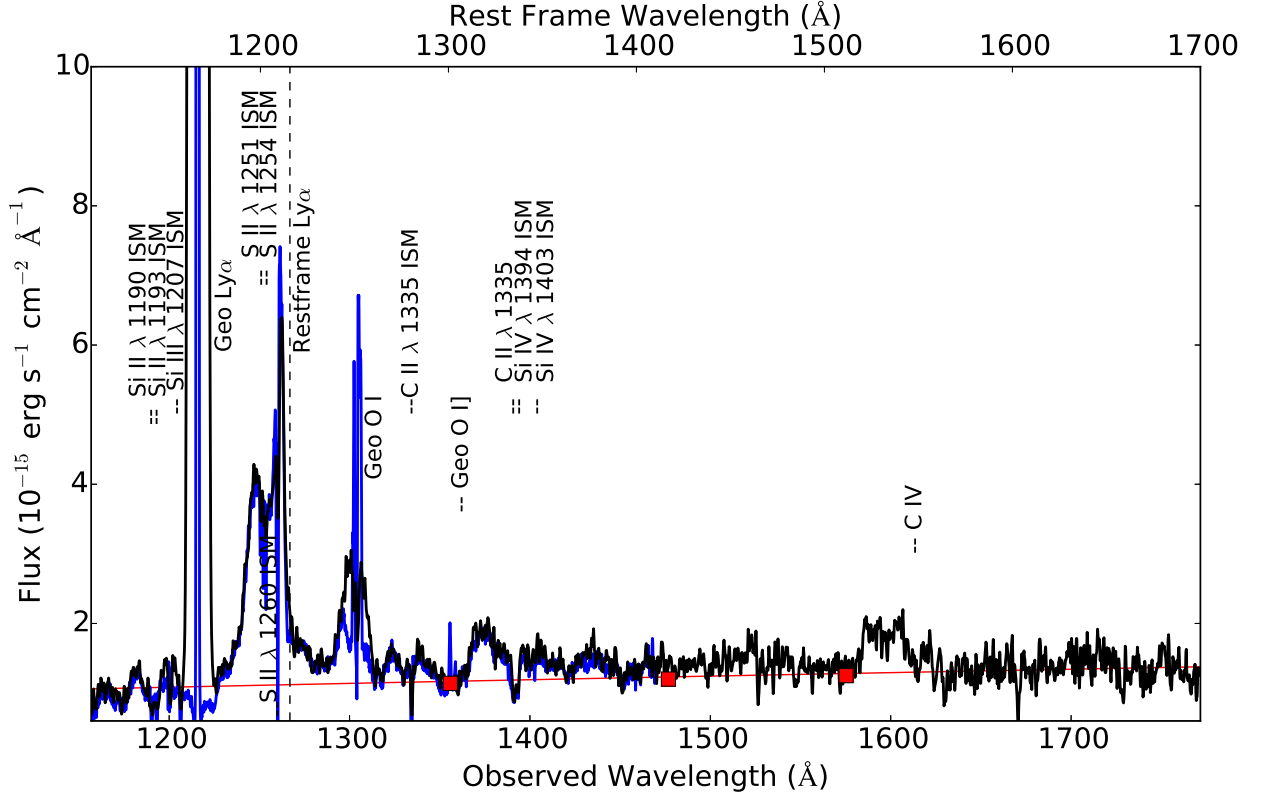


FIG. 1.— *HST*-COS FUV spectra of Mrk 231, obtained in Cycle 19 (blue) and Cycle 21 (black), binned to the same effective resolution to help with the comparison. These spectra have not been corrected for the small foreground Galactic extinction ( $A_V \sim 0.03$  mag.). These spectra, taken  $\sim 3$  years apart, are remarkably similar. They are both dominated by broad, highly blueshifted  $\text{Ly}\alpha$  emission (the vertical dashed line indicates the rest-frame position of  $\text{Ly}\alpha$ ). Broad and highly blueshifted C IV emission is also detected in the Cycle 21 spectrum. The FUV continuum emission is nearly featureless and only slowly declining at shorter wavelengths, consistent with  $f_\lambda \propto \lambda^{0.7}$  (shown as a red line in the lower spectrum). It is dominated by the AGN and only slightly affected by dust reddening ( $A_V \sim 0.5$  mag.; Paper I).

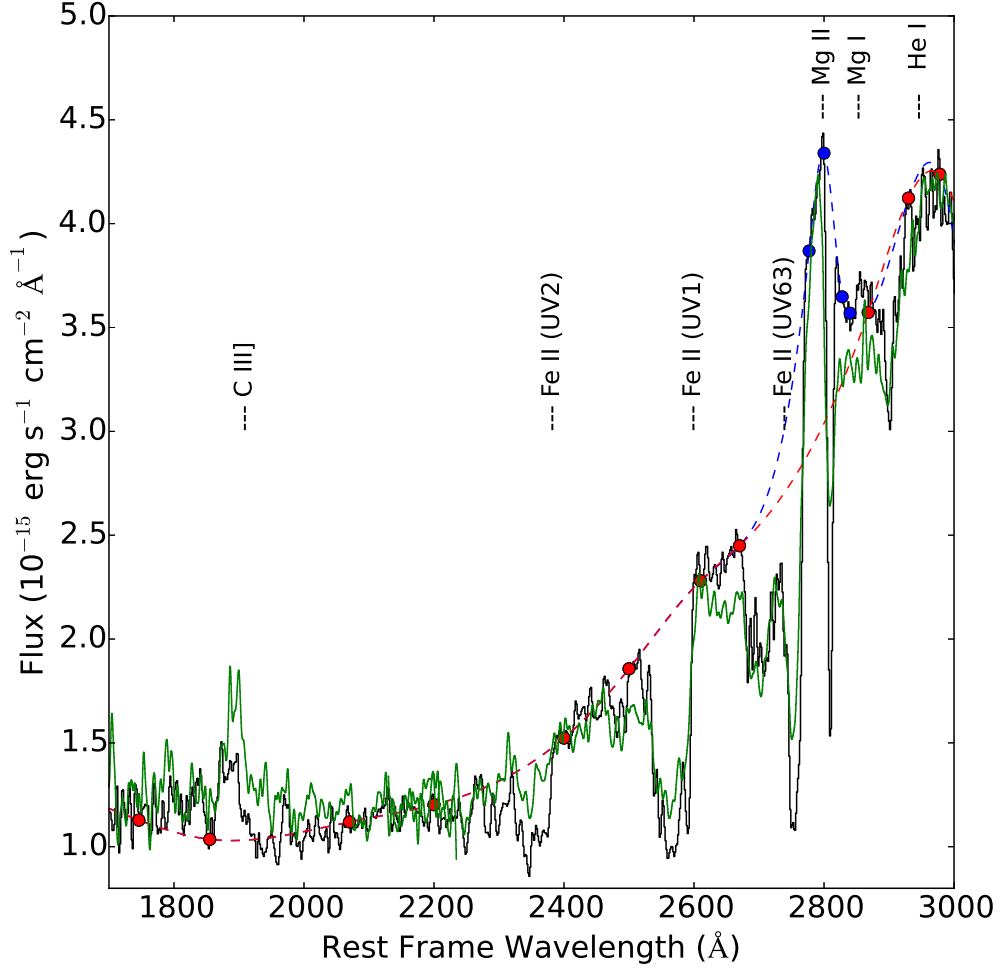


FIG. 2.— *HST*-STIS NUV spectrum of Mrk 231 obtained in Cycle 21. The STIS spectrum (shown in black) was lightly smoothed with a Gaussian kernel with a sigma (width) of 2 spectral pixels to help show the fainter features. The pre-COSTAR FOS spectra from Smith et al. (1995) are shown in green for comparison. The FOS G190H and G270H spectra were heavily smoothed and scaled to account for light losses due to pre-COSTAR aberrations and reproduce the spectrum shown in Figure 1 of Smith et al. The NUV spectrum of Mrk 231 is dominated by strong broad and blueshifted absorption-line features from He I, Mg I, Mg II, and the Fe II UV1, UV2, and UV62/63 multiplet transitions (the vertical dashed marks indicate the expected rest-frame positions of the resonant lines in these features). Broad and highly blueshifted C III] emission is also detected. The blue and red dashed curves represent the pseudo-continuum fits that were used to determine the properties of the broad absorption and emission features, respectively (see Table 1).

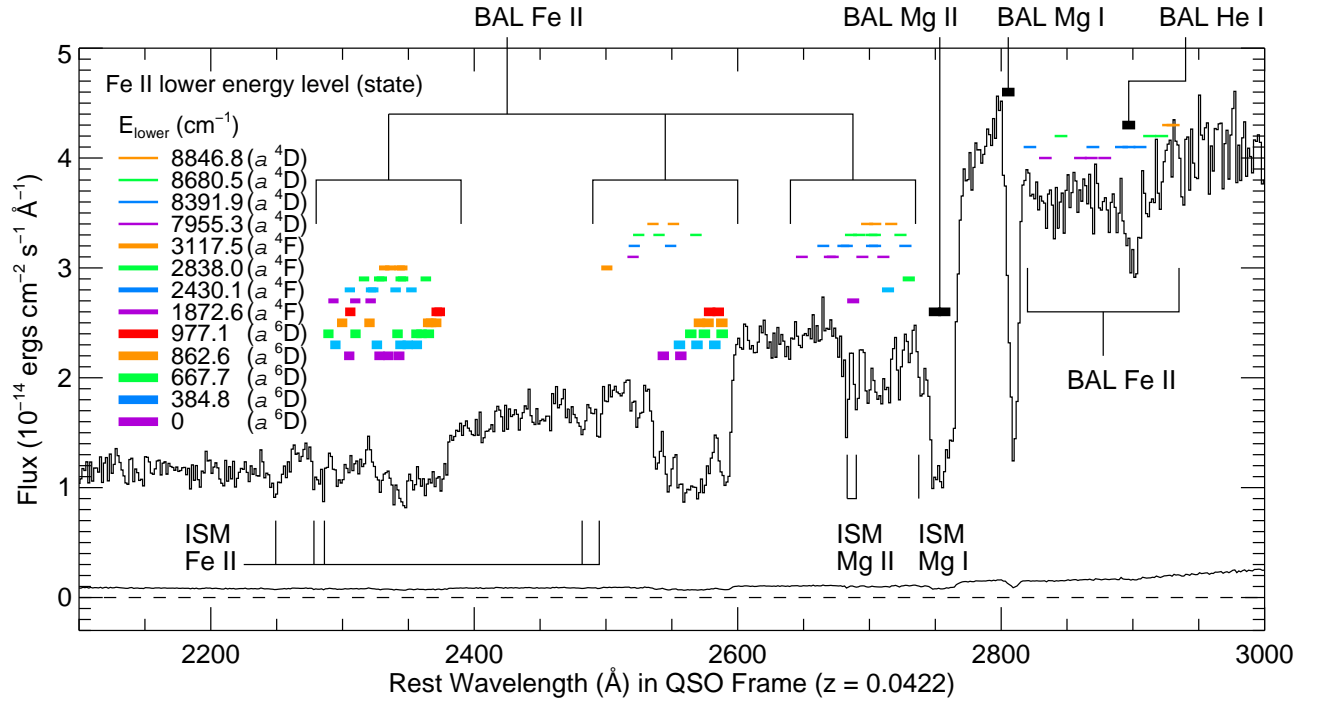


FIG. 3.— The Cycle 21 STIS NUV spectrum of Mrk 231 is labeled to indicate the many transitions contributing to the Fe II multiplets. The thickness of each line indicates the lower state of each transition while the colors indicate the lower fine-structure energy level of each transition. The thickest lines are transitions arising from the  $a^6D$  ground state, intermediate-thickness lines arise from the metastable  $a^4F$  lower state, and the thinnest lines arise from the higher energy metastable  $a^4D$  state. Also labeled on this figure are the positions of the BAL features from He I, Mg I, and Mg II, and the narrow features produced by the Galactic ISM.



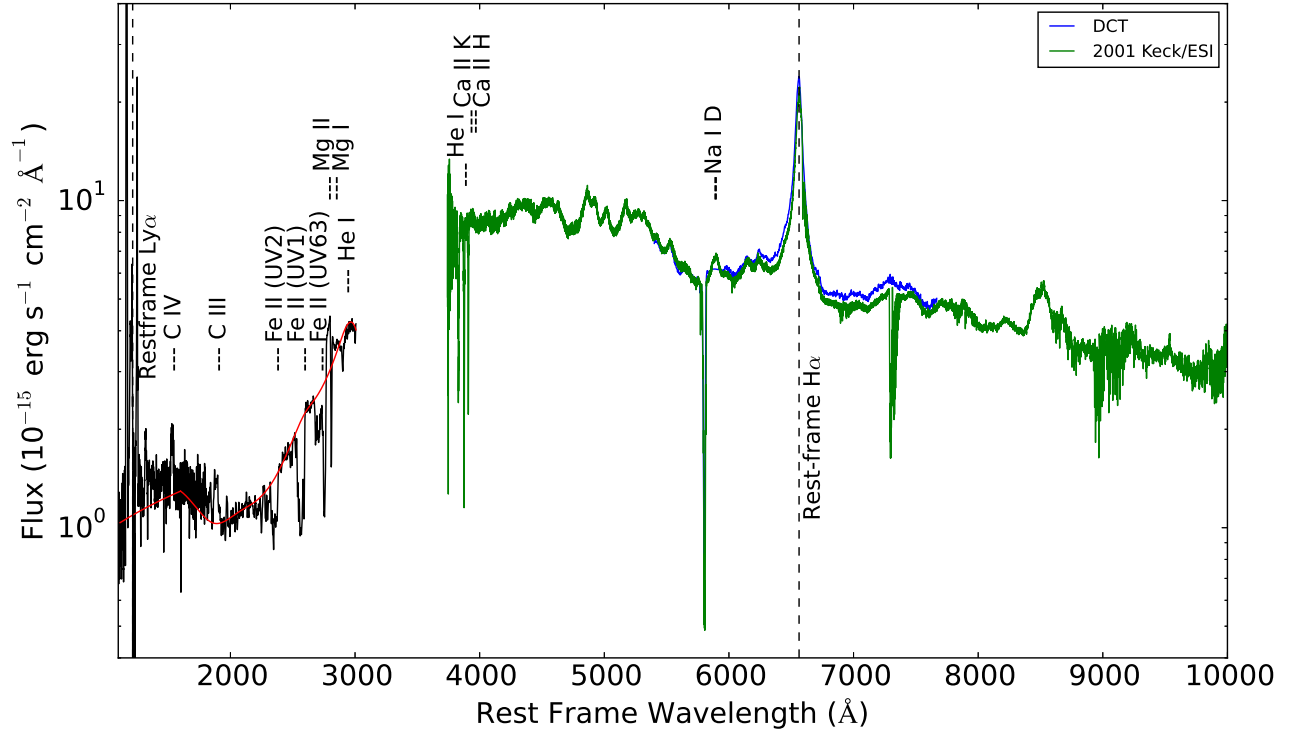


FIG. 4.— The UV – optical spectral energy distribution (SED) of Mrk 231 in  $\log f_\lambda$  versus  $\log \lambda$ (rest-frame) units. This SED combines the new Cycle 21 COS and STIS data with the 2015 DCT (blue) and 2001 Keck/ESI (green) optical spectra. Note the dramatic upturn in flux above  $\sim 2200$  Å. The vertical dash lines indicate the expected rest-frame positions of the main spectral features. The red curve is the same as in Figure 1: it represents the pseudo-continuum used to measure the properties of the various FUV – NUV absorption features (Table 1). The discrepancy in flux between the DCT and Keck spectra at  $6000 - 8000$  Å reflects errors in the flux calibration of the DCT data (which were acquired under non-photometric conditions).

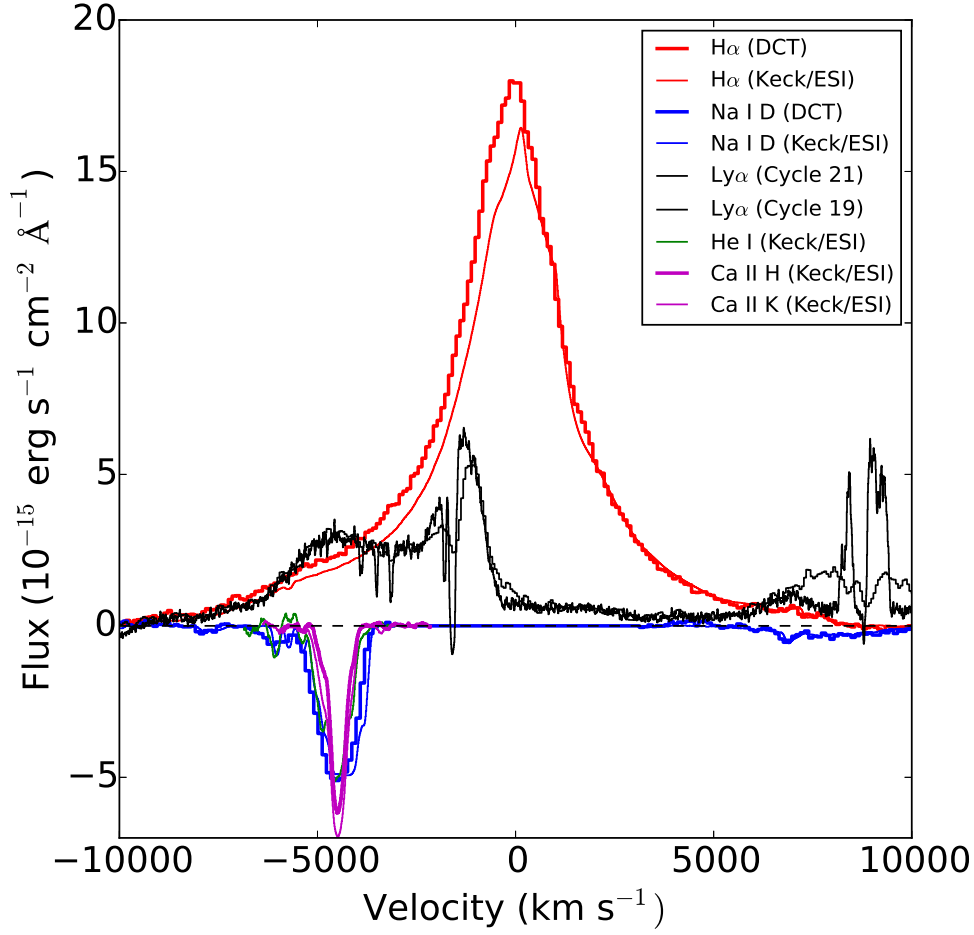


FIG. 5. — Comparison of the continuum-subtracted  $H\alpha$  emission (red),  $Ly\alpha$  emission (black),  $Na\ I\ D$  absorption (blue),  $He\ I^*\ \lambda 3889$  absorption (green),  $Ca\ II\ H\ \lambda 3968$  (thin pink), and  $Ca\ II\ K\ \lambda 3934$  absorption (thick pink). All spectral features are on the same velocity and absolute flux scales. In all cases, the histograms represent the most recent *HST* and DCT spectra while the smooth curves are from the old Keck optical data ( $H\alpha$ ,  $Na\ I\ D$ ,  $He\ I$ , and  $Ca\ II\ H$  and  $K$ ) or the Cycle 19 *HST*/COS data ( $Ly\alpha$ ). Note that the  $Ly\alpha$  profile at  $\sim 5000 - 10,000\ km\ s^{-1}$  is severely affected by geocoronal  $O\ I$  residuals and is thus unreliable. The  $H\alpha$  profiles in both the DCT and Keck data were interpolated at  $\sim +1000 - 2000\ km\ s^{-1}$  to remove the telluric  $O_2\ \lambda 6850$  band. The slight discrepancy in the  $H\alpha$  profile between the DCT and Keck data reflects errors in the flux calibration of the DCT spectrum (which was acquired under non-photometric conditions). As noted in Paper I,  $Ly\alpha$  shares a stronger kinematic resemblance with the broad and blueshifted  $Na\ I\ D$ ,  $He\ I$ , and  $Ca\ II$  absorption features than with  $H\alpha$  emission. See text and Table 1 for more detail.

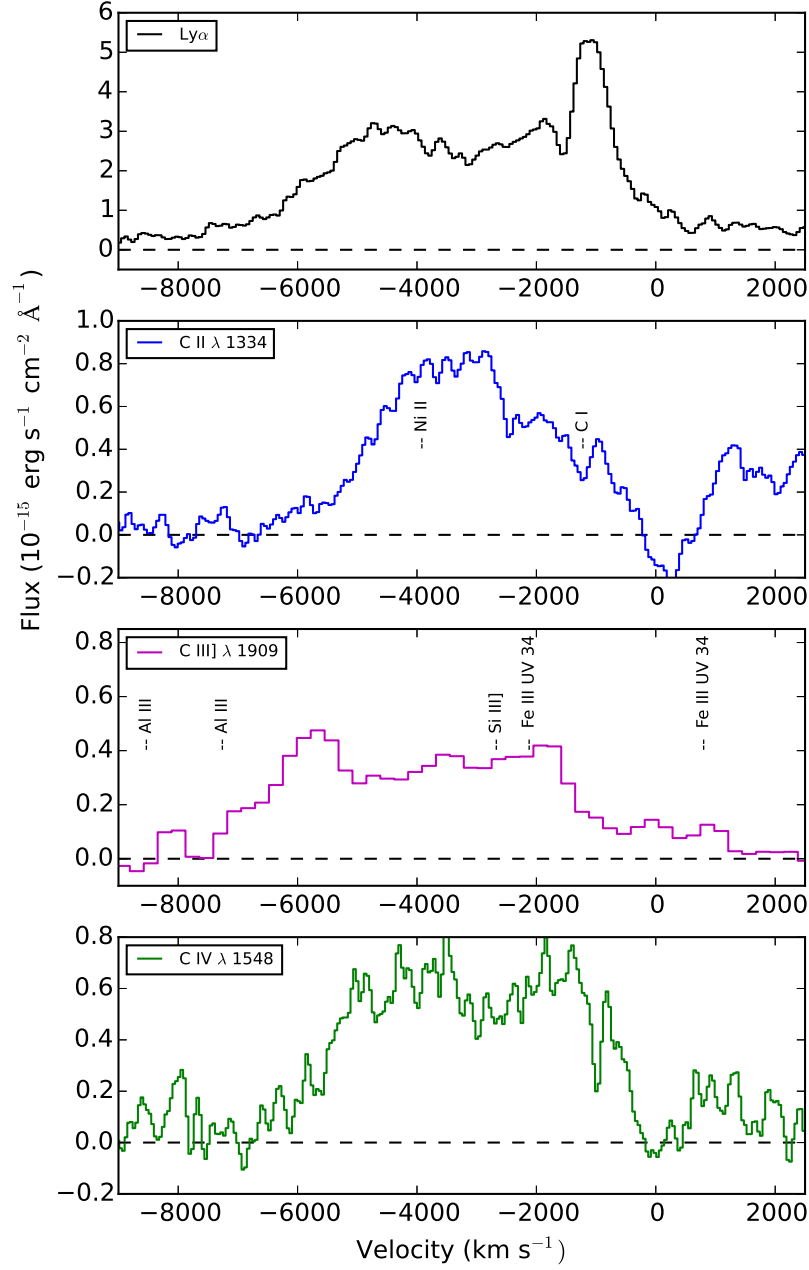


FIG. 6.— Comparison of the continuum-subtracted FUV line emission from Ly $\alpha$  (black), C II  $\lambda$  1334 (blue), C III]  $\lambda$  1909 (red), and C IV  $\lambda$  1548 (green). All four features are on the same velocity scale but the vertical scale has been adjusted to better show the full range of absolute flux. The line labels in the panel showing C III] indicate the  $v = 0$  km s<sup>-1</sup> positions of potentially contaminating features. See text and Table 1 for more detail.



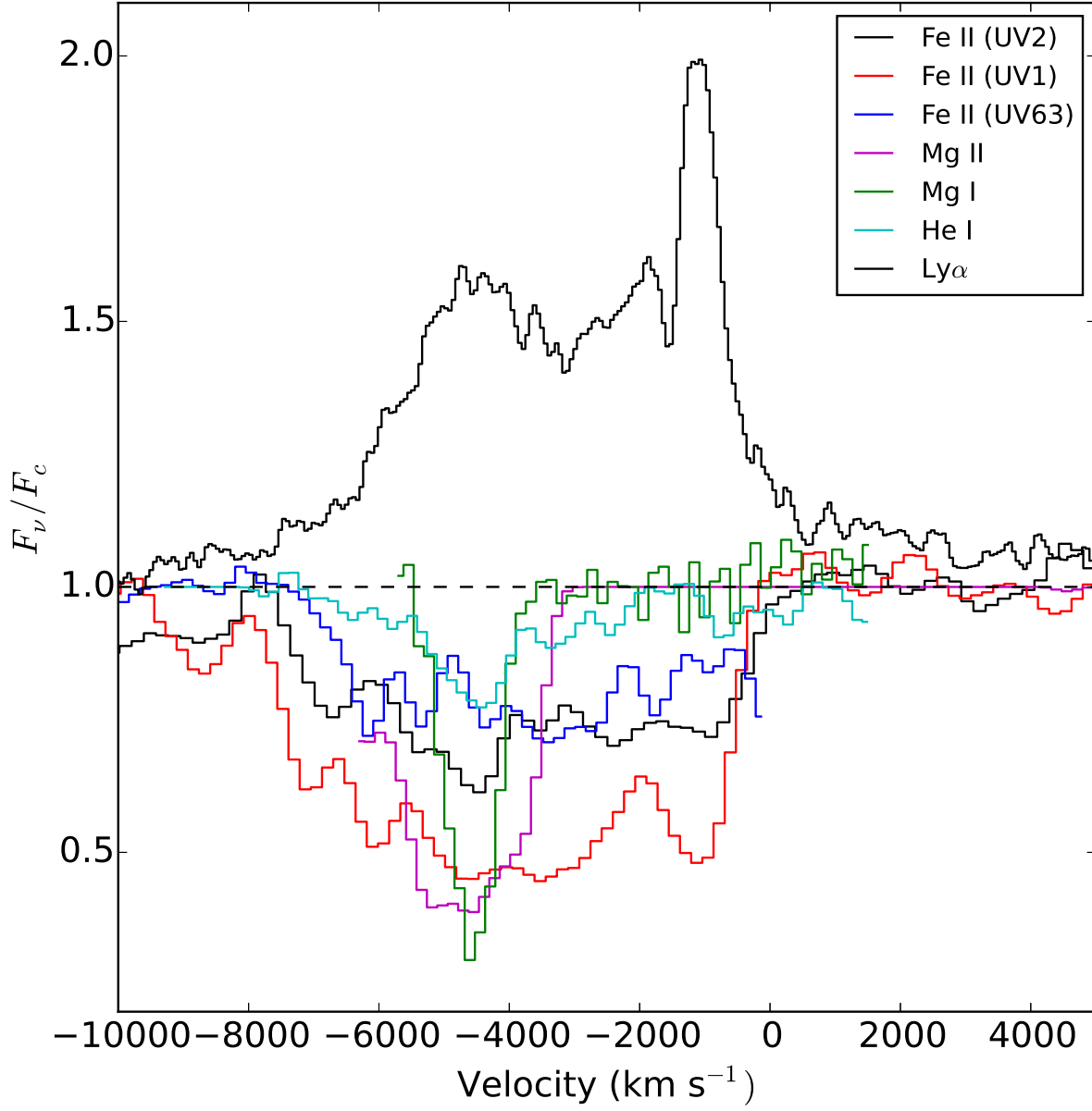


FIG. 7.— Comparison of the continuum-normalized NUV line absorption from Fe II UV2 (black), Fe II UV1 (red), Fe II UV62/63 (blue), Mg II  $\lambda\lambda 2796, 2803$  (pink), Mg I  $\lambda 2853$  (green), and He I  $\lambda 2945$  (turquoise) *versus* the  $\text{Ly}\alpha$  emission profile (black; the peak intensity of  $\text{Ly}\alpha$  was arbitrarily normalized to unity). All of the features are on the same velocity scale. The presence of UV62/63 indicates strong absorption out of level  $\sim 1$  eV above ground and, therefore, all of the fine structure levels in UV1 and UV2 are probably also contributing absorption, not just the one resonance line. This accounts for much of the velocity extent of the Fe II troughs. He I  $\lambda 2945$  also arises from an excited (metastable) state. See text and Table 1 for more detail.

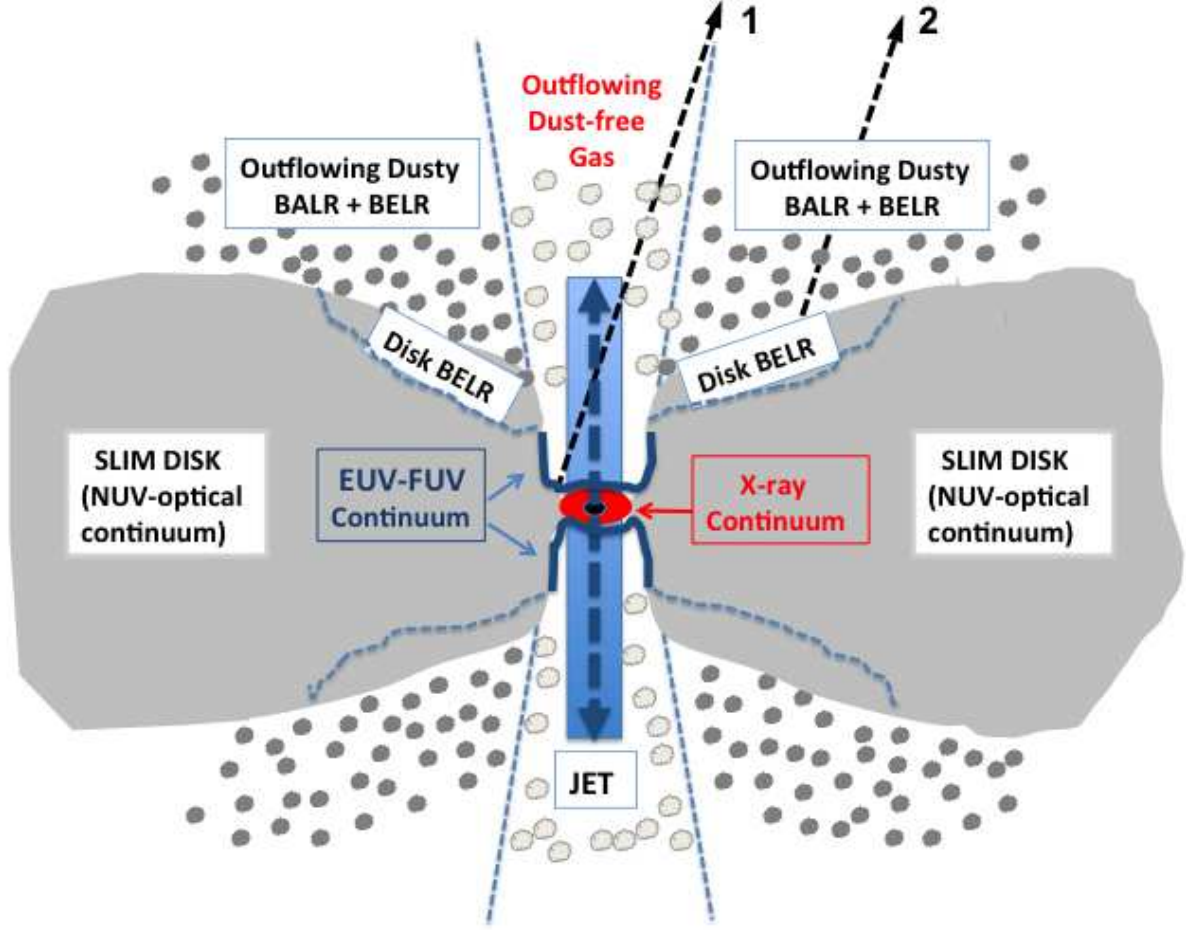


FIG. 8.— Revised geometric disk model of the central  $\sim 10$  pc region of Mrk 231 (not drawn to scale; we warn the readers that this sketch is just meant to be illustrative; it is not accurate in detail). The accretion flow is geometrically thick: it traces a “slim disk” characterized by twin narrow low-density funnels. Our line of sight, shown as two black dashed lines, is constrained to lie  $\sim 10 - 26^\circ$  from the rotation axis based on the high-frequency radio and UV data — our line of sight lies outside of the conical region defined by the near-side funnel but is close enough to the radio jet axis for relativistic boosting to be important. The outflowing dust-free material is highly ionized and not detected in the UV-optical spectrum of Mrk 231, but may contribute to the absorbing column measured in the X-rays. The outflowing dusty clouds act as the low-ionization BALR seen in the NUV-optical and are also responsible for the broad and blueshifted Ly $\alpha$ , C III], and C IV line emission. The BALR is opaque to the underlying FUV continuum emission but lets  $\sim 10\%$  of this emission through, perhaps along the near-side funnel (e.g., line of sight #1 has a direct peek at the FUV source). The line emission from the disk BELR is filtered through the dusty BALR and dominates the optical line emission (e.g., H $\alpha$ ). For clarity the pc-scale double radio structure detected in the VLBA observations is not shown in this image. See Section 4.2 for more detail.